International Journal of Plasticity 129 (2020) 102689

Contents lists available at ScienceDirect

International Journal of Plasticity

journal homepage: www.elsevier.com/locate/ijplas

Comparative modeling of the disregistry and Peierls stress for dissociated edge and screw dislocations in Al

Shuozhi Xu [a,*], Jaber R. Mianroodi [b,c], Abigail Hunter [d], Bob Svendsen [b,c], Irene J. Beyerlein [a,e]

[a] California NanoSystems Institute, University of California, Santa Barbara, CA 93106-6105, USA
[b] Microstructure Physics and Alloy Design, Max-Planck-Institut für Eisenforschung GmbH, Düsseldorf D-40237, Germany
[c] Material Mechanics, RWTH Aachen, Aachen D-54062, Germany
[d] X Computational Physics Division, Los Alamos National Laboratory, Los Alamos, NM 87545, USA
[e] Department of Mechanical Engineering and Materials Department, University of California, Santa Barbara, CA 93106, USA

ARTICLE INFO

Keywords:
Continuum modeling
Dislocations
Phase-field method
Concurrent atomistic–continuum method

ABSTRACT

Many elementary deformation processes in metals involve the motion of dislocations. The planes of glide and specific processes dislocations prefer depend heavily on their atomic core structures. Atomistic simulations are desirable for dislocation modeling but their application to even sub-micron scale problems is in general computationally costly. Accordingly, continuum-based approaches, such as the phase-field microelasticity, phase-field dislocation dynamics (PFDD), generalized Peierls–Nabarro (GPN) models, and the concurrent atomistic–continuum (CAC) method, have attracted increasing attention in the field of dislocation modeling because they well represent both short-range cores interactions and long-range stress fields of dislocations. To better understand their similarities and differences, it is useful to compare these methods in the context of benchmark simulations and predictions. In this paper, we apply the CAC method and different PFDD variants – one of them is equivalent to a GPN model – to simulate an extended (i.e., dissociated) dislocation in Al with initially pure edge or pure screw character in terms of the disregistry. CAC and discrete forms of PFDD are also employed to calculate the Peierls stress. By conducting comprehensive convergence studies, we quantify the dependence of these measures on time/grid resolution and simulation cell size. Several important but often overlooked differences between PFDD/GPN variants are clarified. Our work sheds light on the advantages and limitations of each method, as well as the path towards enabling them to effectively model complex dislocation processes at larger length scales.

1. Introduction

Dislocations, crystalline line defects, are fundamentally associated with the atomic structure of their nanometer-wide cores, within which the atoms are displaced with respect to perfect lattice sites (Cottrell, 2002). While atomistic simulations, via either molecular dynamics (MD) or molecular statics (MS) method, are desirable in modeling dislocations, the large number of degrees of freedom (DOFs) required makes their application to even submicron-scale problems exceedingly computationally expensive (Xu and Chen, 2019). At the other extreme, continuum phenomenological models and crystal plasticity neglect the dislocation core and line discreteness, focusing instead on collective dislocation behavior at and beyond the millimeter scales resulting in slip (Chavoshi

* Corresponding author.
E-mail address: shuozhixu@ucsb.edu (S. Xu).

https://doi.org/10.1016/j.ijplas.2020.102689
Received 30 May 2019; Received in revised form 18 January 2020
Available online 3 February 2020

and Xu, 2019). Classical (i.e., Volterra) continuum dislocation theory neglects the core altogether, and is based on linear elasticity theory which breaks down in the core region.

In the last few decades, numerous continuum modeling approaches have been proposed and applied to study discrete dislocations as lines but without explicitly describing the individual atomic displacements in their cores. In the continuum context, displacements of discrete atoms are approximated by continuous displacement fields, based on which the elastic stress/energy fields outside the dislocation cores can be calculated with the help of linear elasticity. It then follows that either the force applied on each individual dislocation line or the free energy of the dislocation ensemble is calculated and used to drive dislocation motion or to find equilibrium positions of dislocations. For example, in discrete dislocation dynamics (DDD), atoms around dislocations are coarse-grained into discrete lines (Bulatov and Cai, 2006), between which the long-range force-based interactions are dictated via linear elasticity theory while some short-range interactions, e.g., formation and unzipping of dislocation junctions, jogs, and dipoles, may be based on pre-defined criteria (Rhee et al., 1998).

Other continuum modeling approaches, e.g., the phase-field (PF) method (Cahn and Hilliard, 1958; Allen and Cahn, 1979), are energy-based (see e.g., Hohenberg and Halperin, 1977; Provatas and Elder, 2010). In a PF model, the free energy of the system is constructed as a function of order parameters that have difference values for different phases. Then, as the free energy approaches a local minimum, the order parameters at each continuum point are updated and consequently the interfaces between phases move. In general, a "phase" is not limited to the state of matter in thermodynamics, but can represent any "state" in a material, e.g., different lattices (e.g., Levitas, 2018), chemical compositions (e.g., Seol et al., 2003), crystalline grains (e.g., Warren et al., 2003), and cracks in a solid (e.g., Shanthraj et al., 2016, 2017). For dislocation modeling, each phase corresponds to a "state of slip", be it non-slipped, slipped after one dislocation passed, slipped after two dislocations passed, and so on. It follows that dislocations are assumed to evolve such that the free energy of the dislocated system approaches a local minimum.

Similar to PF-based dislocation modeling (e.g., Wang et al., 2001; Koslowski et al., 2002; Shen et al., 2014; Mianroodi and Svendsen, 2015) is that based on the generalized Peierls–Nabarro (GPN) model (Schoeck, 1994). In these, the free energy of a dislocated system is formulated based on, and minimized with respect to, a continuum disregistry field, which is represented by order parameters. Individually in PF- and GPN-based models, different variants have been developed over the years by formulating different initial boundary value problems and employing different numerical solution methods. Physically, PF- and GPN-based models are often equivalent (e.g., Mianroodi et al., 2016). To understand the similarities and differences of such models better, it is important to compare them. Earlier works have clarified the differences between PF models from an analytical point of view (e.g., Wang and Li, 2010). Later, the disregistry/stress fields of edge and screw dislocations calculated with two PF variants, phase-field dislocation dynamics (PFDD) (Koslowski et al., 2002) and atomistic phase-field microelasticity (APFM) (Mianroodi and Svendsen, 2015), have been compared for face-centered cubic (FCC) Al and Au (Mianroodi et al., 2016; Xu et al., 2019b,c). An extension of PFM (Wang et al., 2001), APFM determines the entire energy (i.e., including the gradient energy) atomistically, e.g., with the help of an interatomic potential or density functional theory (DFT). The original PFDD model (Koslowski et al., 2002) did not include the gradient energy in its total energy, making it GPN-like (Mianroodi et al., 2016). Recently, PFDD has been extended to include the gradient energy in the PFDD free energy functional (Xu et al., 2019c). As a result, the extended PFDD model, although mathematically different because it is based on different slip vectors than APFM, is physically equivalent to the latter. In this paper, several PFDD variants will be applied to the same dislocations and their results will be compared. One PFDD variant is equivalent to a GPN model while another is to APFM.

Another continuum-based approach is the concurrent atomistic–continuum (CAC) method (Xiong et al., 2011; Xu et al., 2015). Unlike models in the framework of classical continuum mechanics (CCM), the CAC method has theoretical roots in generalized continuum mechanics (GCM). In CCM, a material is treated as a continuum of material points with infinitesimal size. Each point behaves locally following a constitutive rule, whereas interactions between these points take place only indirectly through the balance equations. At the atomic/nano-scale, however, atoms interact with each other on a complex, multi-dimensional interatomic energy surface, so the locality assumption in CCM no longer holds (Chen and Lee, 2005). Motivated by the limitations of CCM, GCM models that extend the classical field theory to microscopic space and time scales have been proposed (Eringen, 2004). In GCM, a material consists of continuously distributed finite-sized points, each of which has an internal deformation represented by some vectors. Differing in how these vectors are selected, there are many GCM models (Xu et al., 2018c). Atomistic field theory (AFT) (Chen, 2009) is one such model, on which the CAC method is based. AFT concurrently bridges the discrete and continuous descriptions of materials, two fundamentally different viewpoints. Accordingly, the CAC method, as a realization of AFT, coarse-grains atomistic simulations with finite elements, which have much fewer DOFs than equivalent atomistic models. The CAC method has been used to predict the disregistry and Peierls stress of pure edge, pure screw, and mixed-type dislocations in FCC metals (Xu et al., 2015, 2016a, 2018c).

In this paper, we compare simulation results from five PFDD variants and the CAC method in the context of their theoretical aspects, as well as corresponding disregistry field and Peierls stress of a static dislocation of pure edge or pure screw type in Al. A systematic convergence study of the time/grid resolution and simulation cell size in these approaches is provided. Among the PFDD variants, we highlight the effects of (i) whether the gradient energy is included, (ii) determination of the gradient energy coefficients, (iii) whether all slips are confined to the slip plane, and (iv) elastic anisotropy. These four modeling choices are selected because we consider them the most important among all PF dislocation model variants. We remark that the effects of the gradient energy on the disregistry fields were previously quantified (Mianroodi and Svendsen, 2015; Mianroodi et al., 2016; Su et al., 2019b; Xu et al., 2019b,c,d). On the other hand, the Peierls stress, which is closely related to the critical resolved shear stress in an otherwise perfect metal, is also important but was much less studied. To bring validation and reproducibility to the field of dislocation modeling, it is necessary to compare multiple modeling choices in terms of both disregistry and Peierls stress. While this work focuses on their effects on static dislocation core structures, different modeling parameter choices may result in different collective dislocation dynamics, and hence different predicted macroscopic material properties.

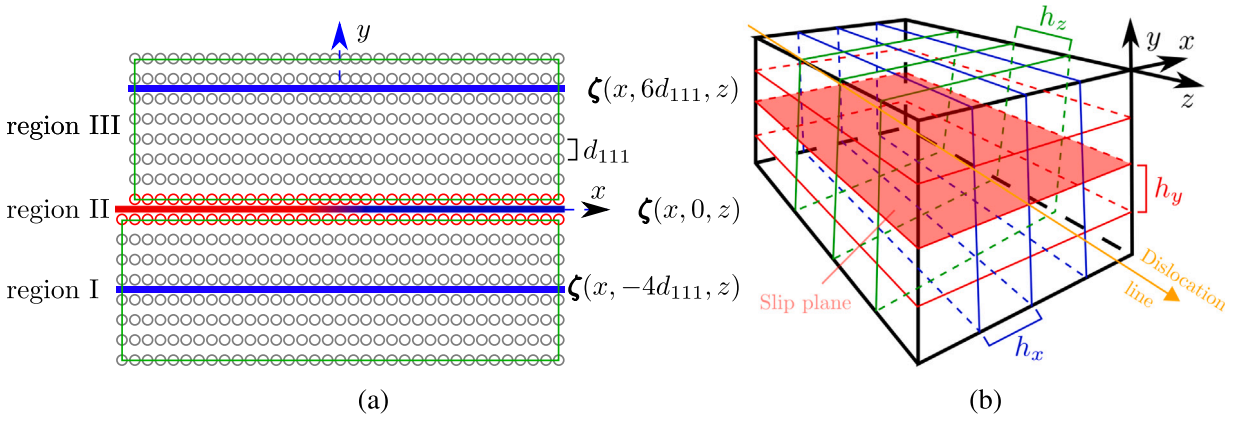

Fig. 1. (a) An illustration of an edge dislocation in a lattice. Atoms are represented by open circles, with those immediately above and below the slip plane ($y = 0$) in red. d_{111} is the distance between two adjacent slip planes. The dislocated system is partitioned into two 3D half-spaces (green boxes), region I and region III, between which there is a 2D flat slab, region II, colored by the magnitude of the disregistry $\boldsymbol{\zeta}$ along the x direction. (b) An illustration of a part of the 3D grid around the dislocation in the PF models. The grid spacings are h_x, h_y, and h_z. The red area and the orange arrow represent the slip plane and the dislocation line, respectively.

2. Theoretical background

In this work, we adopt the following notation. 3D Euclidean vectors are represented by lower-case boldfaced, italicized characters $\boldsymbol{a}, \boldsymbol{b}, \ldots$. Cartesian basis vectors are represented by $\boldsymbol{i}_x, \boldsymbol{i}_y, \boldsymbol{i}_z$. Second rank tensors are represented by upper-case boldfaced, italicized characters $\boldsymbol{A}, \boldsymbol{B}, \ldots$, with $\boldsymbol{I}$ being the second-rank identity matrix. By definition, any $\boldsymbol{A}$ maps any $\boldsymbol{b}$ linearly into a vector $\boldsymbol{Ab}$. $\mathcal{A} \cdot \mathcal{B} = A_{ij\ldots} B_{ij\ldots}$ is the scalar product of two tensors of arbitrary order. Fourth-rank Euclidean tensors $\boldsymbol{\mathcal{A}}, \boldsymbol{\mathcal{B}}, \ldots$ are denoted by upper-case slanted sans-serif characters. By definition, any $\boldsymbol{\mathcal{A}}$ maps any $\boldsymbol{B}$ linearly into a second-order tensor $\boldsymbol{\mathcal{A}B}$. $(\boldsymbol{a} \otimes \boldsymbol{b})\boldsymbol{c} = (\boldsymbol{b} \cdot \boldsymbol{c})\boldsymbol{a}$ defines the dyadic product $\boldsymbol{a} \otimes \boldsymbol{b}$ of $\boldsymbol{a}$ and $\boldsymbol{b}$, $\boldsymbol{A}^{\mathrm{T}}\boldsymbol{b} \cdot \boldsymbol{c} = \boldsymbol{b} \cdot \boldsymbol{Ac}$ defines the transpose $\boldsymbol{A}^{\mathrm{T}}$ of $\boldsymbol{A}$, and $\boldsymbol{\mathcal{A}}^{\mathrm{T}}\boldsymbol{B} \cdot \boldsymbol{C} = \boldsymbol{B} \cdot \boldsymbol{\mathcal{A}C}$ defines the transpose $\boldsymbol{\mathcal{A}}^{\mathrm{T}}$ of $\boldsymbol{\mathcal{A}}$. Finally, let $\mathrm{sym}\, \boldsymbol{A} = (\boldsymbol{A} + \boldsymbol{A}^{\mathrm{T}})/2$ represent the symmetric part of $\boldsymbol{A}$. Additional notations will be introduced as needed in what follows.

2.1. Continuum phase-field (PF) method for the disregistry

Fig. 1a illustrates an edge dislocation in a crystal. This dislocated crystal can be viewed as two 3D half-spaces, regions I and III, separated by a 2D flat slab, region II, lying on the slip plane, the $y = 0$ plane. Since there are usually multiple slip systems in a lattice, a set of n order parameters $\boldsymbol{\phi} = (\phi_1, \ldots, \phi_\alpha, \ldots, \phi_n)$ is introduced for the state of slip. An order parameter ϕ_α can be used for the αth slip system, in which case $\phi_\alpha = 0$ and 1 represent the unslipped and slipped states, respectively. Then, dislocations are the regions occupied by the continuum points with any order parameter having a non-integer value. We emphasize that the state of slip represented by ϕ_α is particular only to the αth order parameter: a continuum point that is slipped in terms of one order parameter may be unslipped in terms of another, and vice versa. Within region II, a sharp interface between the two areas with different states of slip is a dislocation with a planar, compact core. Slip order parameters represent the transition from unslipped to slipped crystal. The FCC lattice, e.g., Al, has a unique misfit energy landscape on {111} slip planes and a {111} dislocation is usually dissociated into two Shockley partial dislocations bounding an intrinsic stacking fault (ISF). Within the context of a PF model, the dissociated dislocation has a finite width, for which $0 < \phi_\alpha < 1$. As the free energy changes, e.g., approaching a local minimum, ϕ_α at each continuum point is updated and consequently the dislocation core evolves.

In our application of the PF models, we restrict attention to single-element FCC materials. Let $\boldsymbol{u}$ represent the displacement field, $\boldsymbol{H} = \nabla \boldsymbol{u}$ the distortion field, $\boldsymbol{E} = \mathrm{sym}\boldsymbol{H}$ the strain field, a_0 the lattice parameter, and b the magnitude of the Burgers vector of a perfect dislocation $\boldsymbol{b} = (a_0/2)\langle 110 \rangle$. The total free energy Ψ is the integration of the free energy density ψ over the entire domain, i.e.,

$$\Psi = \int \psi(x, y, z)\, \mathrm{d}x\, \mathrm{d}y\, \mathrm{d}z\,, \tag{1}$$

where ψ is the sum of the elastic energy density ψ_{ela}, the generalized stacking fault energy (GSFE) density ψ_{gsf}, and the gradient energy density ψ_{gra} (e.g., Wang et al., 2001; Mianroodi and Svendsen, 2015; Xu et al., 2019c), i.e.,

$$\psi(x, y, z) = \psi[\boldsymbol{E}(x, y, z), \boldsymbol{\phi}(x, y, z), \nabla \boldsymbol{\phi}(x, y, z)] = \psi_{\mathrm{ela}}(\boldsymbol{E}, \boldsymbol{\phi}) + \psi_{\mathrm{gsf}}(\boldsymbol{\phi}) + \psi_{\mathrm{gra}}(\nabla \boldsymbol{\phi})\,. \tag{2}$$

In particular,

$$\psi_{\mathrm{ela}}(\boldsymbol{E}, \boldsymbol{\phi}) = \tfrac{1}{2}(\boldsymbol{E} - \boldsymbol{E}_{\mathrm{R}}(\boldsymbol{\phi})) \cdot \boldsymbol{C}_{\mathrm{E}}\, (\boldsymbol{E} - \boldsymbol{E}_{\mathrm{R}}(\boldsymbol{\phi}))\,, \tag{3}$$

$$\psi_{\text{gsf}}(\boldsymbol{\phi}) = \frac{\gamma_{\text{gsf}}(\boldsymbol{\phi})}{l_{\text{gsf}}}, \tag{4}$$

$$\psi_{\text{gra}}(\nabla\boldsymbol{\phi}) = \sum_{\alpha,\beta=1}^{n} \eta_{\text{g0}}^{\alpha\beta}\, \nabla\phi_\alpha \cdot \boldsymbol{N}_{\alpha\beta} \nabla\phi_\beta, \tag{5}$$

where $\boldsymbol{C}_{\text{E}}$ is the elastic stiffness tensor, $\boldsymbol{E}_{\text{R}} = \text{sym}\boldsymbol{H}_{\text{R}}$ is the residual strain, γ_{gsf} is the GSFE per unit area, l_{gsf} is the interplanar distance between two adjacent slip planes based on which γ_{gsf} is calculated, $\eta_{\text{g0}}^{\alpha\beta}$ are the gradient energy coefficients, and

$$\boldsymbol{H}_{\text{R}}(\boldsymbol{\phi}) = \sum_{\alpha=1}^{n} \frac{b_\alpha \phi_\alpha}{d_\alpha} \boldsymbol{s}_\alpha \otimes \boldsymbol{n}_\alpha, \tag{6}$$

$$\boldsymbol{N}_{\alpha\beta} = \frac{\boldsymbol{b}_\alpha \cdot \boldsymbol{b}_\beta}{d_\alpha d_\beta}[(\boldsymbol{n}_\alpha \cdot \boldsymbol{n}_\beta)\boldsymbol{I} - \boldsymbol{n}_\beta \otimes \boldsymbol{n}_\alpha]. \tag{7}$$

Here, $\boldsymbol{s}_\alpha$ is the slip direction, $\boldsymbol{n}_\alpha$ is the slip plane unit normal, $\boldsymbol{b}_\alpha = b_\alpha \boldsymbol{s}_\alpha$ is the slip vector, and d_α is the interplanar distance between two adjacent slip planes, of the αth order parameter. For a single slip plane in an FCC metal, $l_{\text{gsf}} = d_\alpha = d_\beta = d_{111} = a_0/\sqrt{3}$, where d_{111} is the interplanar distance between two adjacent {111} planes. ψ_{gsf} represents the density of energy stored in stacking faults (e.g., ISF) and partial dislocation (e.g., Shockley partial) cores, while ψ_{gra} the density of energy stored in the latter only. In practice, a 3D grid, e.g., the one illustrated in Fig. 1b, is used for discretization.

When the system is subject to an applied stress $\boldsymbol{\sigma}_{\text{app}}$, the external energy density ψ_{ext} is added to the total energy density, i.e.,

$$\psi_{\text{ext}}(\boldsymbol{\phi}) = \boldsymbol{\sigma}_{\text{app}} \cdot \boldsymbol{E}_{\text{R}}(\boldsymbol{\phi}). \tag{8}$$

The time-dependent Ginzburg–Landau (TDGL) equation is then employed to recursively minimize the system free energy with respect to each ϕ_α, i.e.,

$$\dot{\phi}_\alpha = m_0 [\nabla \cdot \partial_{\nabla\phi_\alpha}\psi_{\text{gra}} - \partial_{\phi_\alpha}(\psi_{\text{ela}} + \psi_{\text{gsf}} + \psi_{\text{ext}})], \tag{9}$$

where the superposed dot denotes the time derivative and the Ginzburg–Landau coefficient m_0 is non-negative and assumed constant here. Once all ϕ_α are determined, the disregistry field ζ_β along the β direction is calculated by

$$\zeta_\beta = \sum_{\alpha=1}^{n_{\text{sp}}} \phi_\alpha\, \boldsymbol{b}_\alpha \cdot \boldsymbol{s}_\beta, \tag{10}$$

where n_{sp} is the total number of order parameters on the slip plane within which the αth order parameter and β direction lie. Here, $\beta = 1$ and $\beta = 2$ represent the directions along and normal to the perfect dislocation Burgers vector, respectively. At each continuum point, the 1×2 disregistry vector $\boldsymbol{\zeta}$ lies within each slip plane. For disregistry calculations, the grid spacing along the slip plane normal is usually d_{111}, while the in-slip-plane grid spacings should be as small as possible.

2.2. Continuum generalized Peierls–Nabarro (GPN) models for the disregistry

Similar to the conventional PF model of a dislocation, a GPN model also divides a dislocated system into two half-spaces separated by a 2D flat slab that lies on the slip plane (Fig. 1a). In the original PN model (Peierls, 1940; Nabarro, 1947), a straight edge dislocation with a planar core can only dissociate along the perfect dislocation Burgers vector direction, i.e., only ζ_1 is predicted. Over the last decades, specifically for dislocations in FCC metals, the original PN model was extended to 2D (i.e., ζ_2 is included) (Schoeck, 1994), to 3D (i.e., the component of $\boldsymbol{\zeta}$ along the $\boldsymbol{n}_\alpha$ direction is considered), for mixed-type dislocation (Joós et al., 1994), and for curved dislocation (Xiang et al., 2008), which are collectively termed GPN models. The free energy in GPN models is often formulated as an explicit function of the disregistry field $\boldsymbol{\zeta}$ or the displacement field $\boldsymbol{u}$, which are equivalent. As shown by Mianroodi et al. (2016), the GPN free energy of Xiang et al. (2008) is physically equal to the homogeneous part of the free energy in PFM-based models (e.g., Wang et al., 2001; Mianroodi and Svendsen, 2015) that are based on order parameters.

In most GPN models (except, e.g., Miller et al., 1998, in which ψ_{gsf} has a non-local kernel), the total energy density consists of ψ_{ela} and ψ_{gsf}, i.e.,

$$\psi(\boldsymbol{E}, \boldsymbol{\phi}) = \psi_{\text{ela}}(\boldsymbol{E}, \boldsymbol{\phi}) + \psi_{\text{gsf}}(\boldsymbol{\phi}). \tag{11}$$

It follows that the energy minimization can be realized by

$$\dot{\phi}_\alpha = -m_0 \partial_{\phi_\alpha}(\psi_{\text{ela}} + \psi_{\text{gsf}} + \psi_{\text{ext}}), \tag{12}$$

when the system is subject to $\boldsymbol{\sigma}_{\text{app}}$. Then Eq. (10) can be adopted to calculate the disregistry. Similar to the PF model, d_{111} is usually taken as the grid spacing along the slip plane normal, while small grid spacings are used within the slip plane.

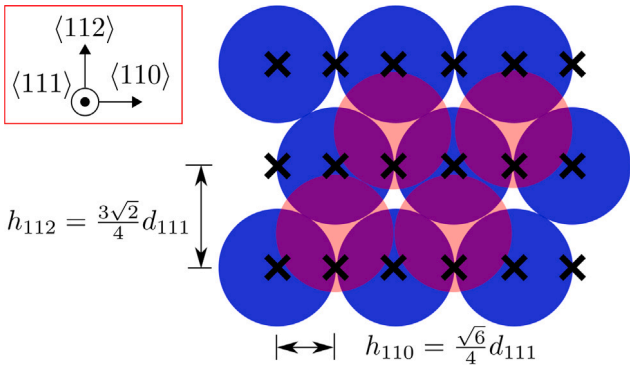

Fig. 2. An illustration of the structured grid points (black crosses) in SVPN overlaid with atoms on two adjacent {111} planes, which are colored in red and blue, respectively. The two atomic spacings within a {111} plane are h_{110} and h_{112}, which are also used as grid spacings in discrete PFDD simulations for the Peierls stress, unless stated otherwise. (For interpretation of the references to color in this figure legend, the reader is referred to the web version of this article.)

2.3. Discrete phase-field (PF) method and semi-discrete variational Peierls–Nabarro (SVPN) models for the Peierls stress

In continuum PF and GPN models, all energy densities (e.g., ψ_{ela} and ψ_{gsf}) are calculated continuously, and the in-slip-plane grid spacings are usually chosen as small as possible to achieve the convergence of the disregistry. However, when these grid spacings approach zero, a rigid dislocation moving in a continuous domain experiences no energy barrier, and hence the Peierls stress is zero. Using a 2D PF model, Hu et al. (2004) found that, when the in-slip-plane grid spacing is sufficiently small, there exists a linear relationship between the dislocation velocity and the applied stress. In other words, the dislocation velocity approaches, but does not equal, zero as the applied stress tends to zero, indicating that there would be no slip resistance. The same was found in the continuum PN model (Peierls, 1940; Nabarro, 1947). One way to circumvent this is to calculate the disregistry first, followed by sampling of the misfit energy (i.e., GSFE in the context of dislocations in FCC systems) at discrete atomic sites (Joós and Duesbery, 1997). Then the Peierls stress is related to the maximum slope of the summed misfit energy (Xiang, 2006). Within the GPN framework, different energy models or sampling methods were developed over the years. For example, in most GPN models, ψ_{gsf} is expressed as a local function of $\boldsymbol{\zeta}$ and sampled on only one side of the slip plane. However, in some versions, ψ_{gsf} is summed over $\boldsymbol{\zeta}$ in a non-local way (Schoeck, 1999) or independently over $\boldsymbol{u}$ on the two atomic rows immediately above and below the slip plane (Lu et al., 2000b). In theory, the same technique could be used to calculate the Peierls stress in continuum PF dislocation models. However, this has not been done in the literature, to our best knowledge.

One drawback of this approach is that it usually predicts an unrealistically high Peierls stress. The inconsistency between the continuous elastic energy and the discrete GSFE also casts doubt on its validity. To address these issues, Bulatov and Kaxiras (1997) proposed a semi-discrete variational PN (SVPN) model, in which both ψ_{ela} and ψ_{gsf} are discretized using finite differencing and numerical integration. A discrete variational method is used to determine the equilibrium discrete nodal disregistries, then the Peierls stress is the critical applied stress at and above which the energy minimization fails. One key ingredient in the SVPN model is that the in-slip-plane grid spacings can no longer be arbitrarily varied for the Peierls stress calculation. Instead, each grid point should correspond to an atom, as illustrated in Fig. 2. While most SVPN models use rectangular grids, one recent model used rhombic grids, which brought the Peierls stress closer to the experimental values by 20%–30% (Edagawa et al., 2019). Similar to the GPN models, only ψ_{ela} are ψ_{gsf} are considered in most SVPN models. However, in a few SVPN variants, an additional non-local energy term (Liu et al., 2017a) or a gradient energy term (Liu et al., 2016; Hale, 2018) is added to the total energy. These are exceptions rather than the norm.

In this work, to calculate the Peierls stress, we formulate the discrete PFDD model, i.e.,

$$\Psi = \sum_{k=1}^{N_z} \sum_{j=1}^{N_y} \sum_{i=1}^{N_x} \psi(x, y, z)\,, \tag{13}$$

where N_x, N_y, and N_z, respectively, are the numbers of grid points along the x, y, and z directions. Here, ψ is no longer the free energy density but the discrete free energy at grid points located at (x, y, z), which correspond to atoms, as shown in Fig. 2. Let the uniform grid spacings along the x, y, and z directions be h_x, h_y, and h_z, respectively. Then within each rectangular cuboid centered at each grid point, i.e., $[x - h_x/2, x + h_x/2) \cap [y - h_y/2, y + h_y/2) \cap [z - h_z/2, z + h_z/2)$, all mechanical quantities, such as disregistry, strain, and stress, are constants. The calculation of ψ follows Eqs. (3)–(7), where $\boldsymbol{E}$, $\boldsymbol{\phi}$, and $\nabla\boldsymbol{\phi}$ (in its central difference form) are values of respective quantities at (x, y, z). Then a discretized TDGL equation, similar to that for a prior SVPN model (Wei et al., 2008), is used to energy minimize the system. We remark that if the same grid spacings are used in the discrete and continuum PFDD models, the calculated disregsitry field would be the same.

One difference between the discrete PFDD model and SVPN is the inclusion of the gradient energy density ψ_{gra} in the former, as demonstrated between Eqs. (2) and (11). As will be discussed in Section 2.4, one PFDD variant we will use will have ψ_{gra} removed. This PFDD variant, termed "PFDD_{ng}", is equal to the SVPN model in its discrete form.

Table 1
A summary of the differences among the five PFDD variants studied in this paper. $\boldsymbol{C}_{\mathrm{E}}$ is the stiffness tensor, ψ_{gra} is the gradient energy density, $\eta_{\mathrm{g0}}^{\alpha\beta}$ are gradient energy coefficients, and $y = 0$ is the slip plane.

	$\boldsymbol{C}_{\mathrm{E}}$	ψ_{gra}	$\eta_{\mathrm{g0}}^{\alpha\beta}$	$\boldsymbol{\phi}(y \neq 0) = \boldsymbol{0}$
PFDD	Anisotropic	Yes	Non-uniform	Yes
$\mathrm{PFDD_{ng}}$	Anisotropic	No	0	Yes
$\mathrm{PFDD_{ugc}}$	Anisotropic	Yes	Uniform	Yes
$\mathrm{PFDD_{nc}}$	Anisotropic	Yes	Non-uniform	No
$\mathrm{PFDD_{iso}}$	Isotropic	Yes	Non-uniform	Yes

2.4. Phase-field disocation dynamics (PFDD) variants

While the same basic framework (Eqs. (2) to (9)) is used for modeling dislocations in PF methods, different variants have been developed due to optional modeling choices. In this paper, we use PFDD as a model method to illustrate three differences among PF variants.

The first difference concerns whether the gradient energy density ψ_{gra} is included. To demonstrate this, the PFDD variant that follows Eq. (11) is termed "$\mathrm{PFDD_{ng}}$". Effects of ψ_{gra} will be discussed in Section 5.1.

The second difference concerns the gradient energy coefficients $\eta_{\mathrm{g0}}^{\alpha\beta}$. By modifying the form proposed by Wang et al. (2001), Shen and Wang (2003) proposed Eq. (5), where $\eta_{\mathrm{g0}}^{\alpha\beta}$ were considered arbitrary parameters. For dissociated dislocations in FCC metals, Mianroodi and Svendsen (2015) fit $\eta_{\mathrm{g0}}^{\alpha\beta}$ to the MS-based Shockley partial dislocation core structure. In one SVPN model, $\eta_{\mathrm{g0}}^{\alpha\beta}$ were fit to the MS-based disregistry fields (Liu et al., 2016). In all these works, a uniform $\eta_{\mathrm{g0}}^{\alpha\beta}$ was adopted for all order parameters. Recently, Xu et al. (2019c) proposed a new PF variant in which $\eta_{\mathrm{g0}}^{\alpha\beta}$ are independently adjustable parameters for each set of $\alpha\beta$. Yet the new PF variant has not been compared with prior variants in which a uniform $\eta_{\mathrm{g0}}^{\alpha\beta}$ was used. In Section 5.2, we will compare the model proposed by Xu et al. (2019c), denoted as "PFDD", with another variant, termed "$\mathrm{PFDD_{ugc}}$", in which a uniform $\eta_{\mathrm{g0}}^{\alpha\beta}$ is fit to the MS-based ISF width associated with the full dislocation.

The third difference is related to an important but often overlooked difference between GPN/SVPN and conventional PF models of dislocations, in terms of which $\boldsymbol{\phi}$ are taken into account. In an FCC lattice, the GPN/SVPN model only takes into account $\boldsymbol{\phi}$ within the {111} slip plane (i.e., $y = 0$ in Fig. 1a), while conventional PF models consider $\boldsymbol{\phi}$ everywhere, including those on non-slip planes (i.e., $y \neq 0$). Appendix shows that $\boldsymbol{\phi}$ may be non-zero on non-slip planes. This is also the case even in a dislocation-free system subject to a small deformation. Strictly speaking, the non-zero $\boldsymbol{\phi}$ at points that are not on the slip plane do not represent the state of slip, so they should not contribute to the free energy of the system via Eqs. (3), (4), (5), and (8). This is the case in the GPN/SVPN models. In Fig. 1a, ψ_{ela} represents the elastic energy stored in regions I and III and ψ_{gsf} represents the GSFE stored in region II. As a result, regions I and III are two Hookean linear elastic continua, while region II is a non-Hookean slab (Wang and Li, 2010). With this view of a dislocated system, sometimes called the "Peierls model", the GPN/SVPN model can be numerically solved using a 1D grid (along the x direction) or a 2D grid (along both x and z directions) within the slip plane.

In contrast, conventional PF models do not confine the energy densities to the slip plane(s). For instance, as illustrated in Fig. 1a, non-zero $\boldsymbol{\phi}(x, y \neq 0, z)$, e.g., $\boldsymbol{\phi}(x, 6d_{111}, z)$ and $\boldsymbol{\phi}(x, -4d_{111}, z)$ are used to calculate non-zero ψ_{ela}, ψ_{gsf}, and ψ_{ext} on these planes, which then add to the total free energy of the system. Consequently, a 3D grid is used and regions I and III are no longer strictly Hookean. This treatment is unphysical because non-zero $\boldsymbol{\phi}(x, y \neq 0, z)$, especially when $|y|$ is large, do not represent dislocations and should not contribute to the free energies densities, e.g., the GSFE density, which represents the density of energy stored within the ISFs and Shockley partial dislocations which only exist inside the slip planes. Following the Peierls model, Shen et al. (2014) formulated a new PF dislocation model, which confines the inelastic displacement to the slip plane, restricts the elastic energy to the two half-spaces, and omits the gradient energy density ψ_{gra}. However, the differences between the new PF model and the conventional one were not quantified. In this paper, a comparison will be conducted in Section 5.3, with ψ_{gra} included in relevant PFDD variants. In what follows, the conventional PF model is termed "$\mathrm{PFDD_{nc}}$", while all other PFDD variants confine all "slip" strictly to the slip plane.

It is also of interest to study the effects of elastic anisotropy on the calculated dislocation properties. Prior atomistic simulations (Rasmussen et al., 1997), a GPN model (Szajewski et al., 2017), and a PFDD model (Xu et al., 2019d) showed that approximating an elastic anisotropic medium as an isotropic one results in an underestimation and overestimation of the ISF width associated with the edge and screw dislocations, respectively. However, it remains unclear, to our best knowledge, how the isotropic approximation influences the Peierls stress. To demonstrate this, we will study another PFDD variant, termed "$\mathrm{PFDD_{iso}}$", in which the material is assumed elastic isotropic.

Differences between the five variants — PFDD, $\mathrm{PFDD_{ng}}$, $\mathrm{PFDD_{ugc}}$, $\mathrm{PFDD_{nc}}$, and $\mathrm{PFDD_{iso}}$ — are summarized in Table 1. As discussed, $\mathrm{PFDD_{ng}}$ is equivalent to GPN, and PFDD is equivalent to APFM. In addition, in its discrete form, $\mathrm{PFDD_{ng}}$ is equivalent to SVPN.

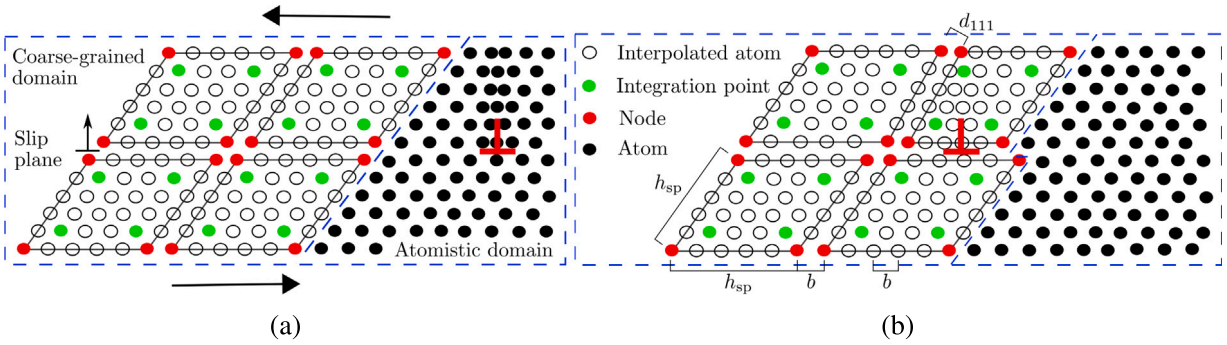

Fig. 3. A 2D CAC simulation cell consisting of an atomistic domain and a coarse-grained domain. In (a), an edge dislocation is located in the atomistic domain. Upon applying a shear stress on the simulation cell, the dislocation migrates into the coarse-grained domain in (b), where the Burgers vector spreads out between discontinuous finite elements, whose edge length is h_{sp}.

2.5. Concurrent atomistic–continuum (CAC) method

The theoretical foundation of the CAC method is AFT, which views a crystal as a continuous collection of lattice points; embedded within each point is a unit cell containing a group of discrete atoms (Xiong et al., 2015). In other words, a two-level crystalline materials description in solid state physics, i.e., crystal structure = lattice + basis, is employed (Xiong et al., 2016). AFT differs from other GCM models in that its sub-level structure and physical description are not continuous but discrete (Chen et al., 2011). In terms of Eulerian coordinates, AFT has the following balance equations (Chen, 2006, 2009; Chen et al., 2018), i.e.,

$$\frac{\mathrm{d}\rho^a}{\mathrm{d}t} = -\rho^a(\nabla_{\boldsymbol{r}} \cdot \boldsymbol{v} + \nabla_{\Delta \boldsymbol{r}^a} \cdot \Delta \boldsymbol{v}^a), \tag{14}$$

$$\rho^a \frac{\mathrm{d}}{\mathrm{d}t}(\boldsymbol{v} + \Delta \boldsymbol{v}^a) = \nabla_{\boldsymbol{r}} \cdot \boldsymbol{T}^a + \nabla_{\Delta \boldsymbol{r}^a} \cdot \boldsymbol{S}^a + \boldsymbol{f}^a_{\mathrm{ext}}, \tag{15}$$

$$\rho^a \frac{\mathrm{d}e^a}{\mathrm{d}t} = \nabla_{\boldsymbol{r}} \cdot \boldsymbol{q}^a + \nabla_{\Delta \boldsymbol{r}^a} \cdot \boldsymbol{j}^a + \boldsymbol{T}^a \cdot \nabla_{\boldsymbol{r}}(\boldsymbol{v} + \Delta \boldsymbol{v}^a) + \boldsymbol{S}^a \cdot \nabla_{\Delta \boldsymbol{r}^a}(\boldsymbol{v} + \Delta \boldsymbol{v}^a), \tag{16}$$

where $\boldsymbol{r}$ is the physical space coordinate of the continuously distributed lattice; $\Delta \boldsymbol{r}^a$ ($a = 1, 2, \ldots, N_a$ with N_a being the total number of atoms in a unit cell) is the subscale internal variable corresponding to the position of atom a relative to the mass center of the lattice located at $\boldsymbol{r}$; ρ^a, $\rho^a(\boldsymbol{v} + \Delta \boldsymbol{v}^a)$, and $\rho^a e^a$ are respectively, the local density of mass, linear momentum, and total energy; $\boldsymbol{v}$ is the velocity vector of the lattice point $\boldsymbol{r}$; $\boldsymbol{v} + \Delta \boldsymbol{v}^a$ is the atomic-level velocity vector of atom a; $\boldsymbol{f}^a_{\mathrm{ext}}$ is the external force vector applied on atom a; $\boldsymbol{T}^a$ and $\boldsymbol{q}^a$ are, respectively, the stress tensor and heat flux vector contributed by atom a due to the homogeneous distortion of the lattice; $\boldsymbol{S}^a$ and $\boldsymbol{j}^a$ are, respectively, the stress tensor and heat flux vector resulting from the reorganization of atoms within the unit cells.

For monatomic crystals like Al, $N_a = 1$, $\Delta \boldsymbol{r}^a = \boldsymbol{0}$, and $\Delta \boldsymbol{v}^a = \boldsymbol{0}$. Consequently, the balance equations reduce to those in CCM (Xu et al., 2018a), i.e.,

$$\frac{\mathrm{d}\rho}{\mathrm{d}t} = -\rho \nabla_{\boldsymbol{r}} \cdot \boldsymbol{v}, \tag{17}$$

$$\rho \frac{\mathrm{d}\boldsymbol{v}}{\mathrm{d}t} = \nabla_{\boldsymbol{r}} \cdot \boldsymbol{T} + \boldsymbol{f}_{\mathrm{ext}}, \tag{18}$$

$$\rho \frac{\mathrm{d}e}{\mathrm{d}t} = \nabla_{\boldsymbol{r}} \cdot \boldsymbol{q} + \boldsymbol{T} \cdot \nabla_{\boldsymbol{r}} \boldsymbol{v}. \tag{19}$$

AFT is applicable to a wide range of nano/micro-scale thermal and mechanical problems in various monatomic and polyatomic crystalline materials. In practice, AFT-based methods partition the simulation cell into two domains: an atomistic domain and a coarse-grained domain, with the interatomic potential as the only constitutive rule (Xu et al., 2016d). In the atomistic domain, $\boldsymbol{r}$ is the atomic position and Eq. (18) is the Newton's second law. Hence, the atoms are updated in the same way as in MD or MS (Xu et al., 2016b). In the coarse-grained domain, realizations of AFT differ in how the balance equations are numerically solved. Specifically for dislocation modeling, the CAC method employs finite elements, while requiring neither displacement continuity nor strain compatibility between them, as illustrated in Fig. 3. As a result, discontinuities may form between finite elements (Xu et al., 2017b). For these discontinuities to be dislocations, all surfaces of the finite elements should lie on the slip planes of the lattice, e.g., the {111} planes in an FCC lattice (Xu et al., 2017a). The CAC method equipped with these finite elements is shown to be useful to explore problems in which full atomistic resolution is required in some regions (e.g., lattice defects), with coarse-graining employed elsewhere to support representation of dislocation interactions and transport (Xu et al., 2017c, 2019a). In this paper, we focus on the modeling of dislocations between finite elements in the coarse-grained domain.

Table 2
Values of some material parameters determined from the EAM potential (Mishin et al., 1999) as discussed in the text. The lattice constant a_0 is in units of Å; the elastic constants C_{11}, C_{12}, C_{44} are in units of GPa.

a_0	C_{11}	C_{12}	C_{44}
4.05	113.80	61.55	31.60

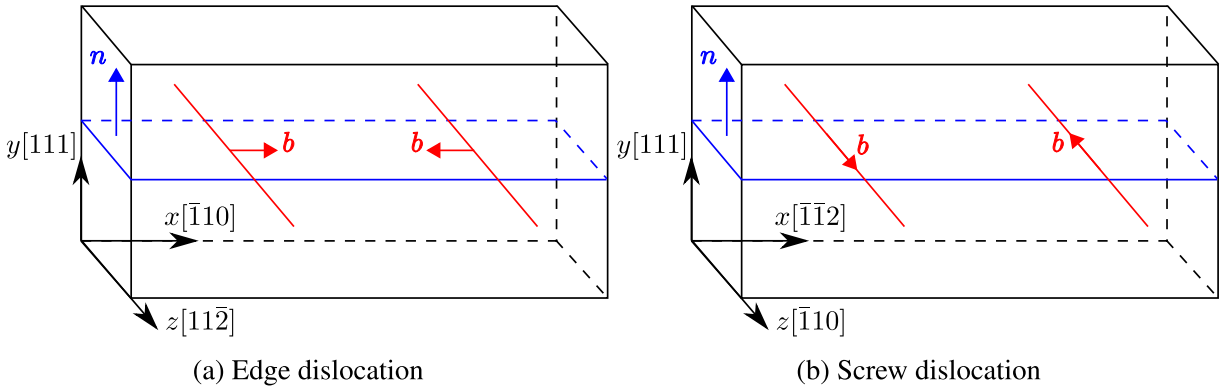

Fig. 4. Simulation box set-up for dissociation of (a) an edge dislocation dipole and (b) a screw dislocation dipole.

3. Simulation set-up

In this section, we present the set-up used in MS, CAC, and PFDD simulations for a static dislocation of pure edge or pure screw type in Al. For comparability of all simulation results, we use the same embedded-atom method (EAM) potential (Mishin et al., 1999), which was shown to agree well with DFT calculations in terms of the ISF energy in Al (Zimmerman et al., 2000). The EAM potential is used for the interatomic interactions in MS and CAC simulations, and for material properties needed in PFDD free energy models, including lattice constant a_0, elastic constants C_{11}, C_{12}, C_{44}, gradient energy coefficients $\eta_{g0}^{\alpha\beta}$, and GSFE per unit area γ_{gsf}. The first four parameters are summarized in Table 2.

A dislocation dipole consisting of two dislocations of the same type but with opposite Burgers vector is built into a 3D periodic simulation cell, as illustrated in Fig. 4. Let L_x, L_y, and L_z be the edge length of the cell along the x, y, and z directions, respectively. The two dislocation lines lie on the mid-y plane and are separated by $L_x/2$ along the x direction. In all simulations, the dislocated system is subject to energy minimization, during which each dislocation, referred to as a monopole in what follows, extends on the mid-y plane. In all cases, we calculate the disregistry fields of dislocations under zero applied stress, i.e., $\boldsymbol{\sigma}_{app} = \mathbf{0}$. In selected cases, we also calculate the Peierls stress of the dislocation, σ_P, which is the minimum resolved shear stress required to translate a dislocation (Peierls, 1940).

A convergence analysis of the time/grid resolution and simulation cell size in PFDD variants and MS/CAC will be conducted in Section 4. A comparison between different PFDD variants will be presented in Section 5. Whenever possible, the same spatial resolution and simulation cell size are used in PFDD and MS/CAC to facilitate quantitative comparison.

3.1. MS and CAC simulations

MS and CAC simulations are carried out by LAMMPS (Plimpton, 1995) and PyCAC (Xu et al., 2018b; Xu and Chu, 2017), respectively. In all MS simulation cells, $L_x = 2L_y$; for the edge and screw dipoles, respectively, $L_z = 9\sqrt{2}/2d_{111}$ and $3\sqrt{6}d_{111}$. Unless stated otherwise, $L_y = 252d_{111}$, in which case an MS simulation cell contains 622,944 and 719,712 atoms, respectively, for the edge and screw dipoles. We will show in Section 4.2 that the simulation cell size used in the calculations to follow is sufficiently large. In CAC models, a coarse-grained domain with uniformly sized 3D rhombohedral finite elements is employed. The Galerkin method is used to convert the balance equations to a set of integration equations, wherein the integrations are approximated by Gaussian quadrature (Xu et al., 2016c). The integration errors were studied by Xu et al. (2015).

Unlike MS simulations in which atoms are assumed volumeless, the finite elements used in CAC bring discretization errors. The edge length of a finite element, h_{sp}, is related to the number of atoms it contains, N_{at}, by $N_{at} = (h_{sp}/b+1)^3$. Unless stated otherwise, $N_{at} = 125$ and $h_{sp} = 4b$. In Section 4.4, the discretization errors will be quantified by identically varying h_{sp} of all finite elements between $4b$ and $10b$, while keeping the interplanar distance between two adjacent finite elements as d_{111}. CAC models have the same L_x and L_y as MS, while L_z is set as $2h_{sp}$.

To calculate the disregistry fields under zero stress, an undissociated perfect dislocation dipole is first created by applying the corresponding isotropic elastic displacement fields to all atoms/nodes. Then conjugate gradient relaxation is carried out and is terminated when one of the following two criteria is satisfied: (i) the change in energy between successive iterations divided by the

most recent energy magnitude is less than or equal to 10^{-15} and (ii) the length of the global force vector for all atoms/nodes is less than or equal to 10^{-15} eV/Å.

To directly calculate the Peierls stress in MS/CAC, the simulation cell is initially loaded to shear stress of $\sigma_{yz} = \sigma_{zy} = 28$ MPa and $\sigma_{xy} = \sigma_{yx} = 0.08$ MPa in the screw and edge cases, respectively. All other stress components are set to zero using the Parrinello and Rahman (1981) method. Then the load is gradually increased using box deformation followed by the Parrinello and Rahman (1981) minimization to remove all stress components but the load-related ones. After stress relaxation, the atomic structure is relaxed using the fast inertial relaxation engine (Bitzek et al., 2006). Stress and atomic structure relaxation are repeated in steps of about 0.2 and 0.08 MPa, in the screw and edge cases, respectively. The Peierls stress is measured as the maximum stress the system reaches before dislocation motion and subsequent stress drop.

3.2. PFDD simulations

All PFDD simulations are carried out using a 3D structured grid, as illustrated in Fig. 1b. In all cases, $L_x = 2L_y$, $L_z = 16h_z$, and $h_y = d_{111}$. Unless stated otherwise, $L_y = 252d_{111}$, and the grid spacings are chosen to equate the atomic spacings, i.e., $h_x = \sqrt{6}/4d_{111}$ and $h_z = 3\sqrt{2}/4d_{111}$ for an edge dipole, while $h_x = 3\sqrt{2}/4d_{111}$ and $h_z = \sqrt{6}/4d_{111}$ for a screw dipole, as illustrated in Fig. 2.

The effects of L_x and L_y will be quantified in Section 4.2. In Peierls stress calculations, the grid spacings do not vary because they are fixed in the discrete form (Eq. (13)). In disregistry field calculations, the continuum form is used and selected grid spacings are varied between $0.25d_{111}$ and $10d_{111}$. The effects of the in-slip-plane grid spacings will be independently assessed in Section 4.3. Then following the CAC model, h_x and h_z are collectively termed h_{sp}, whose effects will be explored in Section 4.4. Note that the grid spacing changes by means of varying the number of grid points along the corresponding direction while the simulation cell size is kept largely the same.

The elastic energy density ψ_{ela} is calculated by fast Fourier transform (FFT) method with the help of Green's functions. The slip vector $\boldsymbol{b}_\alpha$ is along a $\langle 110 \rangle$ direction, and there are three order parameters per slip plane. Thus, $n_{\text{sp}} = 3$ and there are nine gradient energy coefficients $\eta_{\text{g0}}^{\alpha\beta}$. Determination of $\eta_{\text{g0}}^{\alpha\beta}$ in different PFDD variants will be discussed in Section 5.2. The Ginzburg–Landau coefficient m_0 is set to unity and the effects of the timestep size Δt will be analyzed in Section 4.1. Note that m_0 and Δt are unitless after all energy densities are nondimensionalized by μ, where $\mu = (3C_{44} + C_{11} - C_{12})/5$ is the isotropic shear modulus in Voigt form.

Initially, an undissociated perfect dislocation dipole is inserted by assigning non-zero ϕ_a to the grid points needed to achieve a given dislocation character. Specifically, $\phi_1 = 1$ and $\phi_2 = \phi_3 = 0$ for the grid points on the mid-y plane between $L_x/4$ and $3L_x/4$. During recursively running the TDGL equation, each monopole becomes extended. To calculate the disregistry fields under zero stress, iterations are terminated when the Euclidean norm of the difference in global vector of each order parameter between successive iterations is smaller than 10^{-5}. Selected PFDD simulations are repeated with a smaller tolerance of 10^{-6}; results are found to differ by about 1%. Based on the disregistry field, the ISF width, d, is defined as the distance between the centers of two Shockley partial dislocations of the same monopole; the center is determined by projecting the disregistry field onto the partial dislocation direction (Xu et al., 2019b).

To determine the Peierls stress σ_{P}, an incremental resolved shear stress $\Delta\sigma_0 = 10^{-5}\mu$ is applied to the dislocated system. In particular, the xy and yx components of the stress tensor $\boldsymbol{\sigma}_{\text{app}}$ are non-zero for the edge dipole, and the yz and zy components of $\boldsymbol{\sigma}_{\text{app}}$ are non-zero for the screw dipole. For each resolved shear stress σ_0, the same convergence criteria mentioned earlier are used to find the equilibrium core structure. When the TDGL equation fails to converge within 20,000 timesteps, the value of σ_0 is recorded, and $\sigma_{\text{P}} = \sigma_0 - \Delta\sigma_0/2$.

As discussed in Section 2.3, PFDD$_{\text{ng}}$ and GPN are equivalent in terms of the formulation, so are discrete PFDD$_{\text{ng}}$ and SVPN. However, our PFDD$_{\text{ng}}$ simulation results may differ from those based on GPN/SVPN due to a different energy minimization scheme and a different method to calculate the elastic energy density. These differences apply in both the disregistry and Peierls stress calculations. Here, in PFDD$_{\text{ng}}$, the TDGL equation (Eq. (12)) and FFT are employed, respectively, for energy minimization and elastic energy calculation. For GPN/SVPN models, a variety of energy minimization schemes were used in the literature, including the conjugate gradient method (Lu et al., 2000a), TDGL equation coupled with the conjugate gradient method (Wei et al., 2008), steepest descent method (Liu et al., 2016), particle swarm optimization (Zhang et al., 2017), Powell's minimization method (Hale, 2018), iterative optimization (Edagawa et al., 2019), and genetic algorithm (Zhang et al., 2019). In terms of the elastic energy calculation, prior GPN/SVPN models used either FFT (Xiang et al., 2008), fast multipole method (Zhu et al., 2015), or the Stroh method (Liu et al., 2016; Hale, 2018). However, it remains unclear how the simulation result may change when different numerical implementations are used. For the current work, we anticipate that PFDD$_{\text{ng}}$ and GPN/SVPN would yield the same result if the TDGL equation and FFT were utilized in the latter.

4. Effects of the time/grid resolution and simulation cell size

In this section, we conduct convergence analyses for the time/grid resolution and simulation cell size in PFDD variants and MS/CAC. Note that the convergence is related to the specific algorithm we employ. For example, if instead the elastic energy density is calculated by the Stroh method, the grid resolution to achieve the convergence may change.

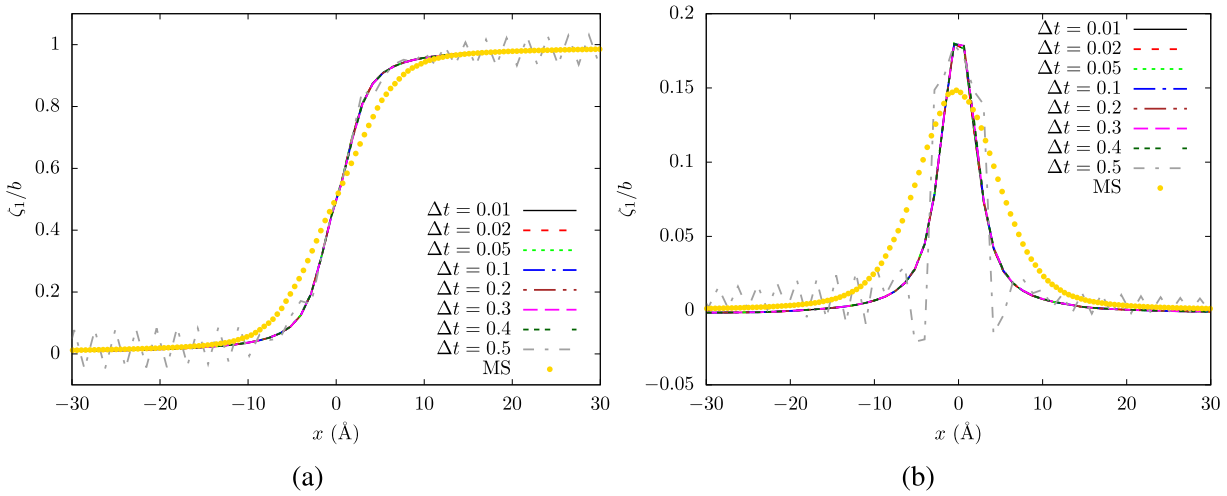

Fig. 5. Disregistry fields of a screw monopole (a) along and (b) normal to the perfect dislocation Burgers vector direction as a function of the timestep size, Δt. Results are based on PFDD_{ng}, with grid spacings $h_x = 3\sqrt{2}/4d_{111}$, $h_y = d_{111}$, and $h_z = \sqrt{6}/4d_{111}$.

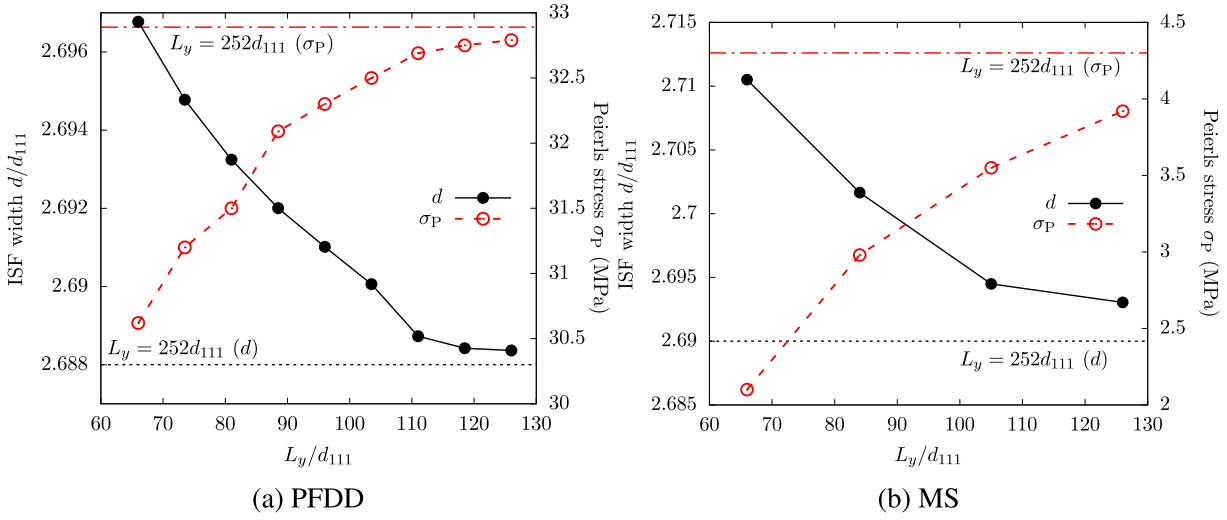

Fig. 6. ISF width d, and Peierls stress σ_{P}, of an edge monopole predicted by (a) PFDD and (b) MS, as function of the simulation cell edge length L_y. In all simulation cells, $L_x = 2L_y$. In PFDD, $L_z = 16h_z$, $h_x = \sqrt{6}/4d_{111}$, $h_y = d_{111}$, $h_z = 3\sqrt{2}/4d_{111}$, and the timestep size $\Delta t = 0.01$. In MS, $L_z = 3\sqrt{6}d_{111}$. Results based on the largest L_y considered are indicated by two horizontal dashed lines. Similar convergence is achieved for the screw monopole.

4.1. Timestep size

In PFDD simulations, the explicit Euler method is employed for the time integration. Take Eq. (12) as an example, the order parameter ϕ_a at time $t_i + \Delta t$ is formulated explicitly based on its value at time t_i, i.e.,

$$\phi_\alpha(t_i + \Delta t) = \phi_\alpha(t_i) - m_0 \, \Delta t \, \partial_{\phi_\alpha(t_i)} \left[\psi_{\text{ela}}(t_i) + \psi_{\text{gsf}}(t_i) + \psi_{\text{ext}}(t_i)\right]. \tag{20}$$

While facilitating numerical implementations, the Euler method is known to require the timestep size Δt to be small enough for numerical stability, which results in long computational time (Gunter et al., 2002). The largest allowable Δt is reduced when the grid spacing decreases, the Ginzburg–Landau coefficient m_0 increases, or the total energy density increases (e.g., when the gradient energy density is included or large gradient energy coefficients are used). With $m_0 = 1$, it is shown in Fig. 5 that the largest Δt for energy convergence within individual PFDD_{ng} simulation is 0.4 for a screw monopole. However, further reducing Δt yields different disregistry fields from that of $\Delta t = 0.4$, suggesting that the results do not actually converge in terms of Δt. We find that, the true timestep size convergence is achieved when $\Delta t \leq 0.05$. Hence, to ensure solution convergence in all PFDD simulations, $\Delta t = 0.01$ is used in the remainder of this paper.

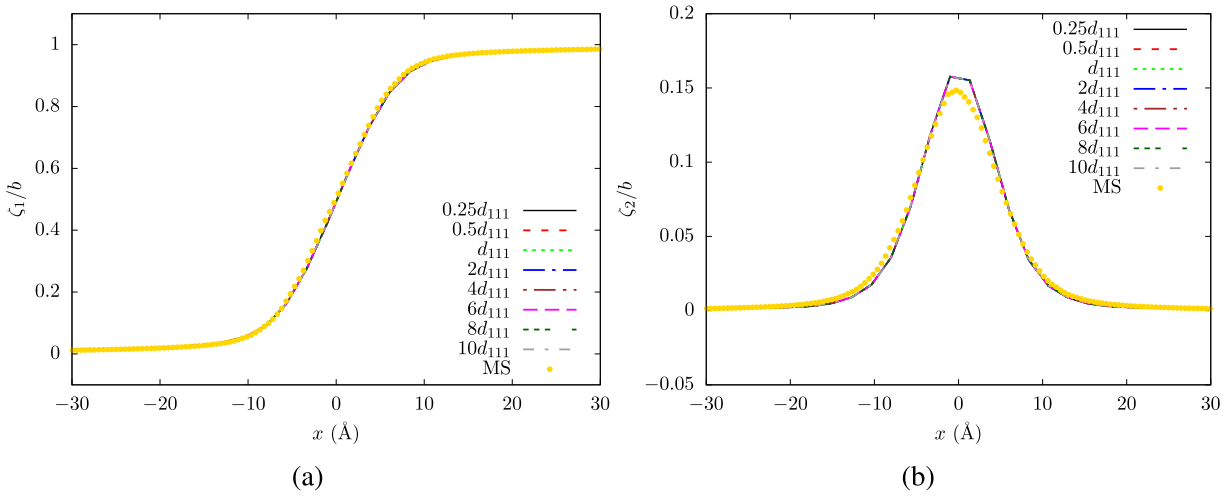

Fig. 7. Disregistry fields of a screw monopole (a) along and (b) normal to the perfect dislocation Burgers vector direction as a function of the grid spacing along the dislocation line, h_z. Results are based on PFDD, with grid spacings $h_x = 3\sqrt{2}/4d_{111}$ and $h_y = d_{111}$ and the timestep size $\Delta t = 0.01$.

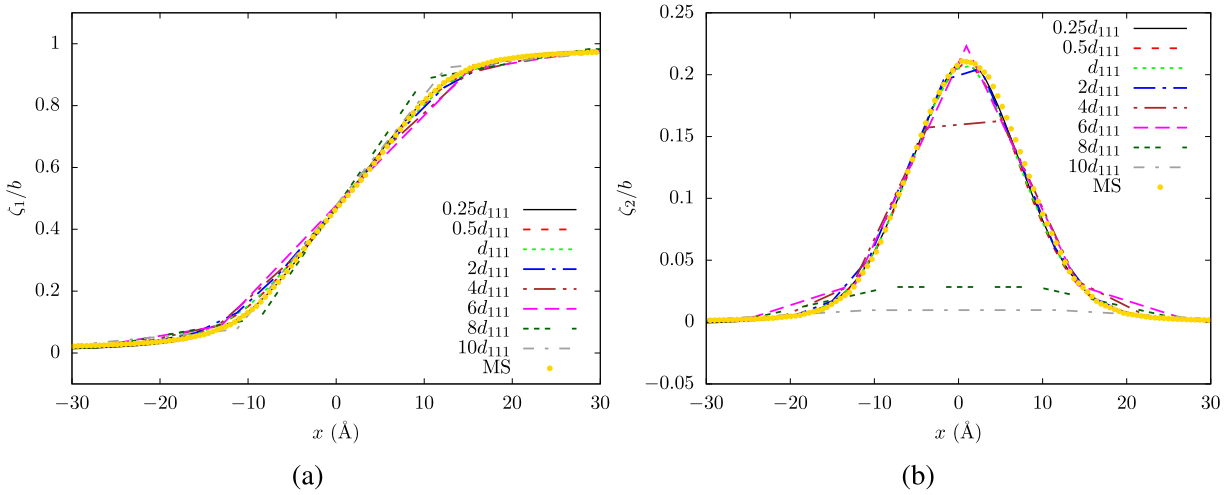

Fig. 8. Disregistry fields of an edge monopole (a) along and (b) normal to the perfect dislocation Burgers vector direction as a function of the grid spacing within the slip plane and normal to the dislocation line, h_x. Results are based on PFDD, with grid spacings $h_y = d_{111}$ and $h_z = 3\sqrt{2}/4d_{111}$ and the timestep size $\Delta t = 0.01$.

4.2. Simulation cell size

Here, we quantify the effects of the simulation cell size in PFDD and MS/CAC. As mentioned in Section 3, PFDD and MS/CAC simulations in this work adopt $L_x = 2L_y$ and $L_z = 16h_z$. Hence, we vary L_y from $66d_{111}$ to $252d_{111}$. Fig. 6a shows that, as L_y increases, the ISF width d and Peierls stress σ_P decreases and increases, respectively. In PFDD, both quantities converge to stable values when $L_y \geq 111d_{111}$. Similar trend is observed in MS simulations, as shown in Fig. 6b. The simulation cell size dependence is an outcome of the long-range interactions between the two opposite-signed dislocations in a dipole. In the remainder of this paper, $L_y = 252d_{111}$ will be used in all PFDD and MS/CAC simulations.

4.3. Two independent grid spacings within the slip plane

Here, we investigate using PFDD the effects of the two in-slip-plane grid spacings, h_x and h_z, separately. Fig. 7 shows the disregistry field of a screw monopole and the finding that it does not vary with the grid spacing along the dislocation line, h_z. This suggests that, if a dislocation is expected to remain straight during a PFDD simulation, e.g., enforced by the periodic boundary conditions, a large h_z can be used along the line direction to reduce the number of DOFs in the cell. In Fig. 8, we see that the disregistry field is almost invariant with respect to h_x when $h_x \leq d_{111}$, but the peak value of ζ_2 decreases rapidly as h_x increases

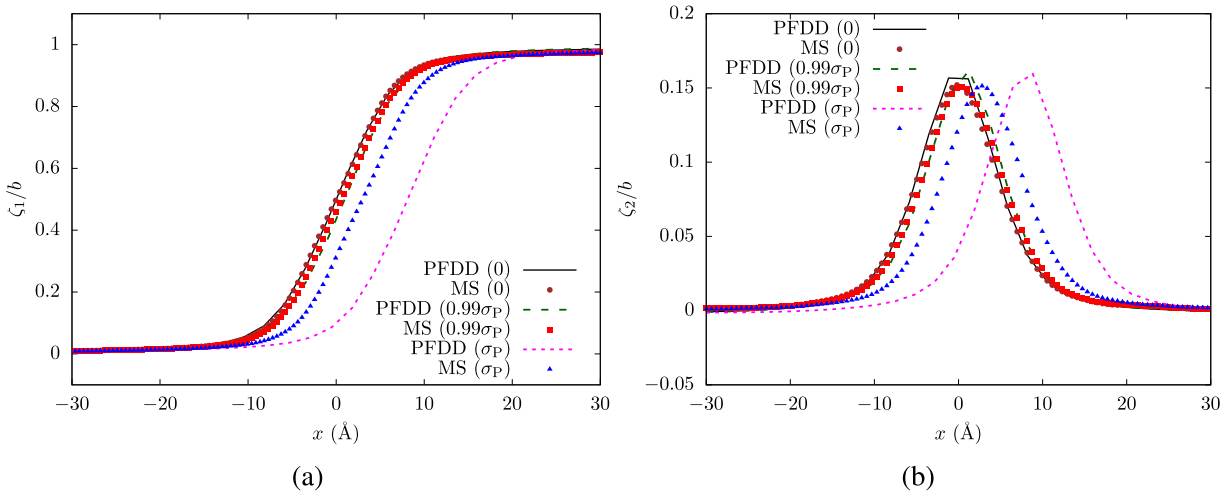

Fig. 9. Disregistry fields of a screw monopole (a) along and (b) normal to the perfect dislocation Burgers vector direction, subject to three applied stresses: 0, $0.99\sigma_P$, and σ_P. In PFDD, grid spacings $h_x = 3\sqrt{2}/4d_{111}$, $h_y = d_{111}$, and $h_z = \sqrt{6}/4d_{111}$, and the timestep size $\Delta t = 0.01$.

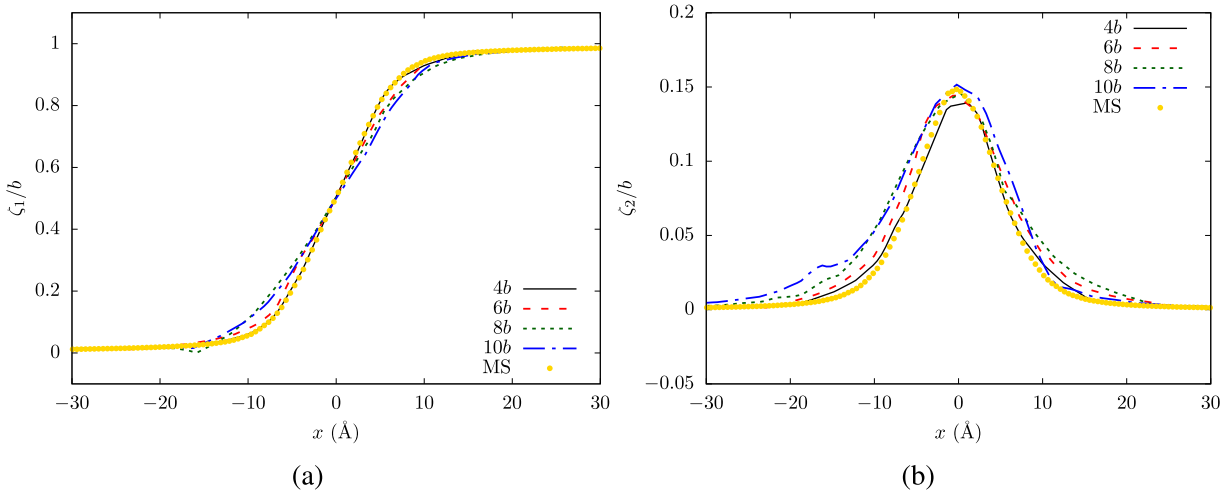

Fig. 10. Disregistry fields of a screw monopole (a) along and (b) normal to the perfect dislocation Burgers vector direction, as a function of the grid spacing within the slip plane, $h_{sp} = h_x = h_z$. Results are based on CAC, with the grid spacing $h_y = d_{111}$.

when $h_x \geq 4d_{111}$, suggesting that the monopole becomes more compact. Such behavior is expected because once the grid spacing is large enough, the dislocation core will sit in between grid points. Overall, we find that h_x dominates the influences of the grid spacings within the slip plane. We emphasize that both h_{110} and h_{112} (illustrated in Fig. 2) are close to or smaller than d_{111}, suggesting that the disregsitry is indeed converged when these two grid spacings are used.

For a screw dipole with $h_x = 3\sqrt{2}/4d_{111}$ and $h_z = \sqrt{6}/4d_{111}$, Fig. 9 shows that, subject to a resolved shear stress of $0.99\sigma_P$, the disregistry profile is displaced slightly but its shape is almost unchanged in both PFDD and MS, in agreement with prior SVPN and MD calculations (Liu et al., 2017b,a). As shown in Table 3, even with the same grid spacing, PFDD still yields a higher σ_P than MS. Better agreement may be achieved by using FCC-like grids (Ruffini et al., 2017) in PFDD.

4.4. A uniform grid spacing within the slip plane

Here, h_x and h_z are collectively termed h_{sp}, whose effects are analyzed in PFDD and CAC. In PFDD, we find that the effects of h_{sp} are identical to those of h_x, i.e., the monopole becomes compact when $h_{sp} \geq 4d_{111}$. This result is expected because h_x dominates the effects of the in-slip-plane grid spacing. In CAC, disregistry fields largely maintain their shape when h_{sp} is varied. In particular, the dislocation remains dissociated even when $h_{sp} = 10b$, as shown in Fig. 10. Moreover, σ_P decreases as h_{sp} increases, as shown in Fig. 11b. This finding agrees with a previous CAC work (Xu et al., 2016a) in which, with $h_{sp} = 12b$, σ_P calculated in CAC was

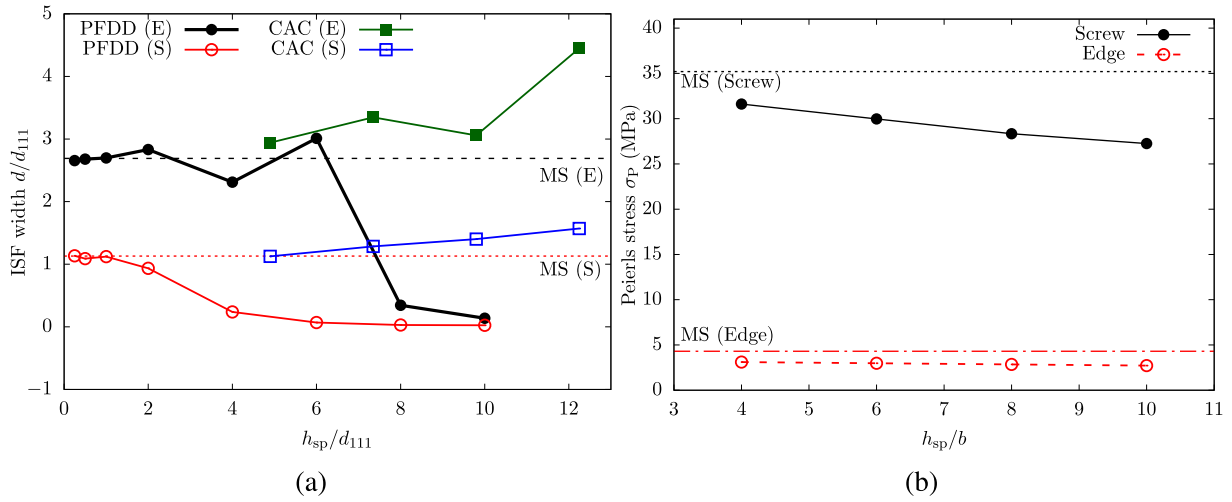

Fig. 11. (a) ISF widths, d, predicted by PFDD and CAC simulations, for both edge (E) and screw (S) monopoles; the MS-based results are indicated by two horizontal dashed lines. (b) Peierls stress σ_P calculated in CAC simulations as a function of the edge length of finite elements, h_{sp}. MS-based Peierls stresses are 35.2 MPa and 4.3 MPa for the screw and edge dislocations, respectively.

Table 3
ISF widths d (in units of d_{111}) and Peierls stresses σ_P (in units of MPa) of the edge (E) and screw (S) dislocations calculated in the five PFDD variants summarized in Table 1. The same grid spacings as in SVPN models are used: $h_y = d_{111}$; for the edge dipole, $h_x = \sqrt{6}/4d_{111}$ and $h_z = 3\sqrt{2}/4d_{111}$, and for the screw dipole, $h_x = 3\sqrt{2}/4d_{111}$ and $h_z = \sqrt{6}/4d_{111}$. The timestep size $\Delta t = 0.01$. For PFDD-based results, d are $\pm 0.5h_x$ and σ_P are $\pm 5 \times 10^{-6}\mu = 0.15$ MPa.

	MS	PFDD	PFDD_{ng}	PFDD_{ugc}	PFDD_{nc}	PFDD_{iso}
d (S)	1.13	1.13	0.59	1.13	1	1.18
d (E)	2.69	2.69	1.48	2.69	2.6	2.68
σ_P (S)	35.2	77.85	132.27	67.27	118.07	78.75
σ_P (E)	4.3	19.73	31.91	16.72	20.97	23.09

approximately 75% of that based on MS. It is an outcome of the linear shape/interpolation function used in the finite elements in the coarse-grained domain in CAC.

5. A comparison between different PFDD variants

Section 4 established that, for the PFDD-based results to be comparable with those from atomistics, a sufficiently small timestep size, a sufficiently large simulation cell, and grid spacings with atomic resolution should be applied. In this section, we focus on comparing the five PFDD variants summarized in Table 1. Main results are summarized in Table 3 and Fig. 12. Unless stated otherwise, in what follows, $\Delta t = 0.01$, $L_x = 2L_y$, $L_y = 252d_{111}$, $L_z = 16h_z$, $h_y = d_{111}$. For the edge dipole, $h_x = \sqrt{6}/4d_{111}$ and $h_z = 3\sqrt{2}/4d_{111}$; for the screw dipole, $h_x = 3\sqrt{2}/4d_{111}$ and $h_z = \sqrt{6}/4d_{111}$.

5.1. PFDD vs. PFDD_{ng}

First, we study the effects of the grid spacing h_{sp} on the disregistry in PFDD_{ng}. Based on a screw monopole, Fig. 13 shows that the disregistry field is almost invariant with respect to h_{sp} when $h_{sp} \leq 0.5d_{111}$ and the monopole becomes more compact when $h_{sp} \geq 2d_{111}$. Recall that these two critical grid spacings are d_{111} and $4d_{111}$, respectively, in PFDD. This suggests that, PFDD_{ng}, or equivalently the GPN models that neglect the gradient energy density ψ_{gra}, requires a finer grid spacing than PFDD, which includes ψ_{gra} in its total energy density. Note that in a prior GPN calculation where the grid was adaptively refined (Zhu et al., 2015), 3 grid points per Burgers vector — equivalently, a grid spacing of $0.41d_{111}$ — were found to be sufficient to achieve convergence for the disregistry field, in agreement with our assessment.

Table 3 shows that, adding ψ_{gra} to the total energy density (i) increases the ISF width d and (ii) decreases the Peierls stress σ_P. Specifically for Al, the former agrees with our prior PF-based work (Xu et al., 2019b,c) while the latter has been reported by Liu et al. (2016). We remark that, introducing ψ_{gra} was recently found to decrease d of the edge dislocations in Ir, Ni, Pd, and Rh (Xu et al., 2019d).

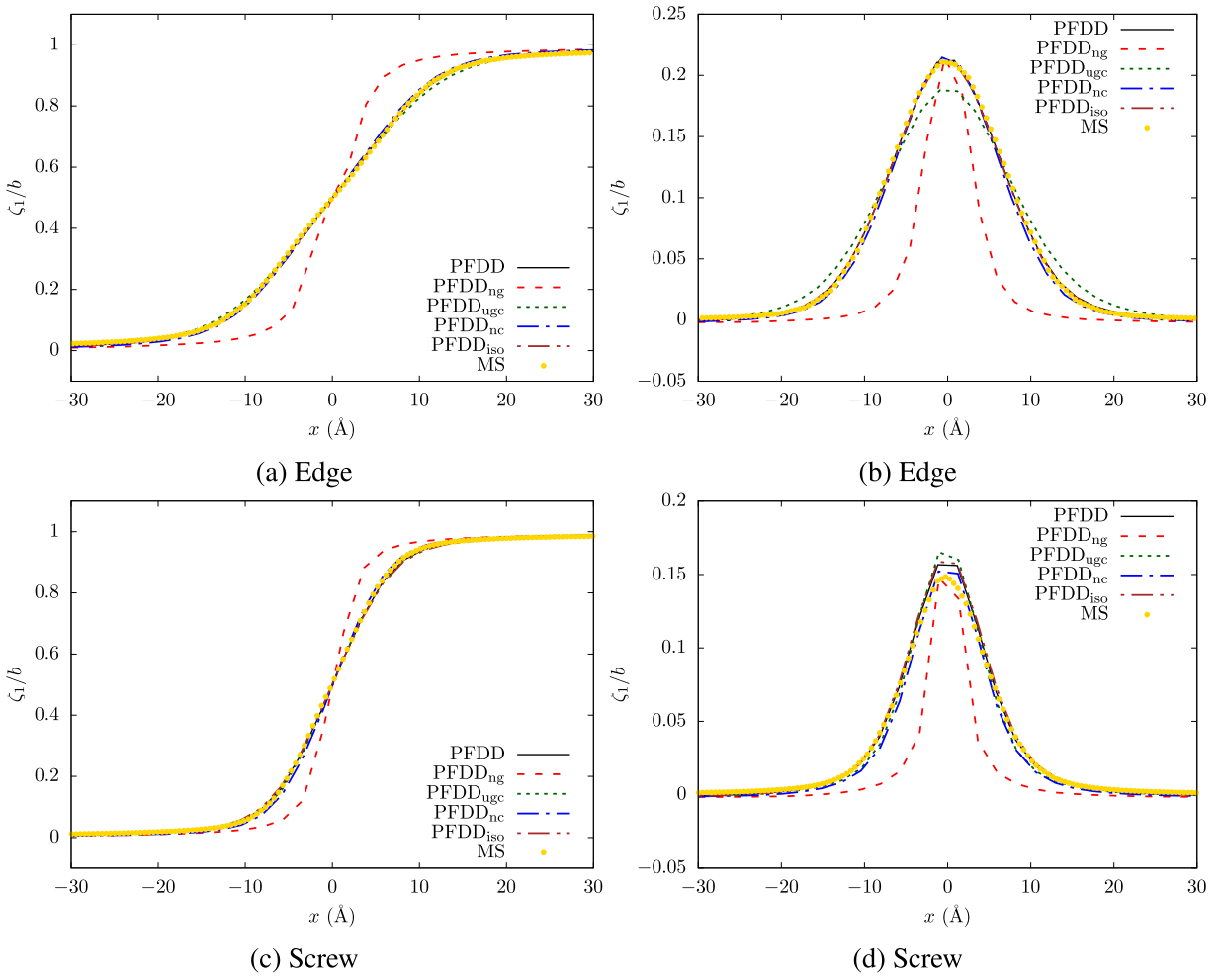

Fig. 12. (a) Disregistry fields of an edge or a screw monopole (a,c) along and (b,d) normal to the perfect dislocation Burgers vector direction. Results are based on MS and the five PFDD variants summarized in Table 1.

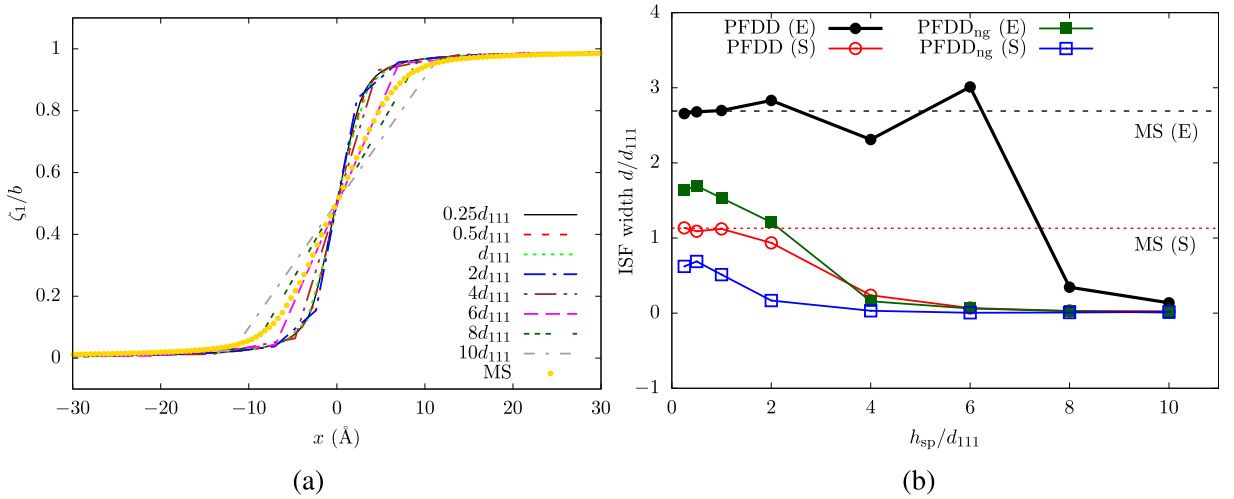

Fig. 13. (a) Disregistry fields of a screw monopole along the perfect dislocation Burgers vector direction, as a function of the grid spacing within the slip plane, $h_{sp} = h_x = h_z$. Results are based on PFDD$_{ng}$, with the grid spacing $h_y = d_{111}$ and the timestep size $\Delta t = 0.01$. (b) ISF widths, d, predicted by PFDD and PFDD$_{ng}$ simulations, for both edge (E) and screw (S) monopoles; the MS-based results are indicated by two horizontal dashed lines.

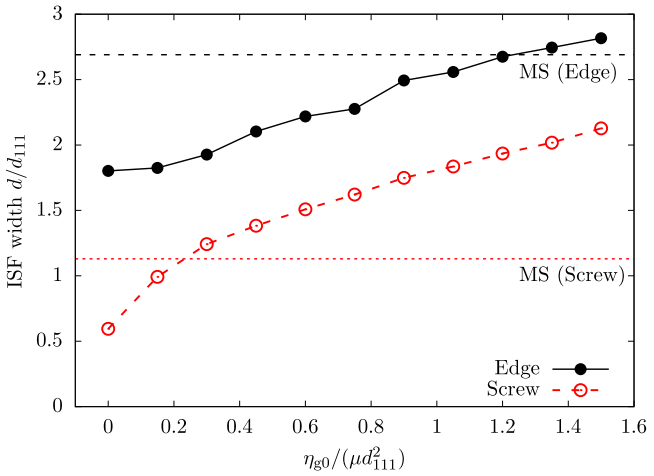

Fig. 14. ISF widths, d, predicted by PFDD$_{ugc}$, for the edge and screw dislocations, with respect to the gradient energy coefficient $\eta_{g0}^{\alpha\beta}$. The timestep size $\Delta t = 0.01$; for an edge dipole, $h_x = \sqrt{6}/4d_{111}$ and $h_z = 3\sqrt{2}/4d_{111}$, while for a screw dipole, $h_x = 3\sqrt{2}/4d_{111}$ and $h_z = \sqrt{6}/4d_{111}$. When $\eta_{g0}^{\alpha\beta} = 0$, PFDD$_{ugc}$ reduces to PFDD$_{ng}$. MS-based results are indicated by two horizontal dashed lines.

Table 4
Values of the gradient energy coefficients (in units of μd_{111}^2) for the edge and screw dislocations in PFDD and PFDD$_{ugc}$. In PFDD, values of $\eta_{g0}^{\alpha\beta}$ are calculated based on η_{g0}^{I} and η_{g0}^{II} via Eqs. (21)–(23).

	PFDD		PFDD$_{ugc}$
	η_{g0}^{I}	η_{g0}^{II}	$\eta_{g0}^{\alpha\beta}$
Screw	0.2667	0.4	0.24
Edge	1.0667	0.4	1.23

5.2. PFDD vs. PFDD$_{ugc}$

Here, we compare two PFDD variants that adopt different gradient energy coefficients $\eta_{g0}^{\alpha\beta}$. For each slip plane, $n_{sp} = 3$ and there are nine gradient energy coefficients $\eta_{g0}^{\alpha\beta}$ with α and β ranging from 1 to 3. However, as discussed by Xu et al. (2019c), only two $\eta_{g0}^{\alpha\beta}$ are independent. In what follows, let them be η_{g0}^{I} and η_{g0}^{II}. They are related to $\eta_{g0}^{\alpha\beta}$ by

$$\eta_{g0}^{11} = \eta_{g0}^{12} = \eta_{g0}^{13} = \eta_{g0}^{21} = \eta_{g0}^{31} = \eta_{g0}^{I}, \tag{21}$$

$$\eta_{g0}^{22} = \eta_{g0}^{33} = \eta_{g0}^{I}/4 + 3\eta_{g0}^{II}/4, \tag{22}$$

$$\eta_{g0}^{23} = \eta_{g0}^{32} = -\eta_{g0}^{I}/2 + 3\eta_{g0}^{II}/2. \tag{23}$$

Traditionally, η_{g0}^{I} and η_{g0}^{II} were assumed the same, and hence a uniform coefficient $\eta_{g0}^{\alpha\beta}$ was used in most prior PF dislocation models. In the literature, there are several ways to calibrate the uniform $\eta_{g0}^{\alpha\beta}$ (Mianroodi and Svendsen, 2015; Liu et al., 2016; Xu et al., 2019d). Here, in PFDD$_{ugc}$, the value of $\eta_{g0}^{\alpha\beta}$ is characterized by fitting the predicted ISF width d to MS, i.e.,

$$\eta_{g0}^{\alpha\beta} = \arg\min \left\{ d(\eta_{g0}^{\alpha\beta}) - d_{MS} \right\}. \tag{24}$$

Specifically, several PFDD$_{ugc}$ simulations are performed with a preassigned $\eta_{g0}^{\alpha\beta}$, ranging from $0.15\mu d_{111}^2$ to $1.5\mu d_{111}^2$. For each coefficient, the ISF width d is obtained and directly compared to that from MS. Fig. 14 shows the variation in d with respect to $\eta_{g0}^{\alpha\beta}$. The values of $\eta_{g0}^{\alpha\beta}$ providing the best agreement are $1.23\mu d_{111}^2$ and $0.24\mu d_{111}^2$ for the edge and screw dipoles, respectively. These values are used in PFDD$_{ugc}$ simulations.

Recently, Xu et al. (2019c) considered η_{g0}^{I} and η_{g0}^{II} as independent variables. Their values can be determined by fitting the predicted disregistry fields to MS, i.e.,

$$[\eta_{g0}^{I}, \eta_{g0}^{II}] = \arg\min \left\{ \zeta(\eta_{g0}^{I}, \eta_{g0}^{II}) - \zeta_{MS} \right\}. \tag{25}$$

The values of the best $[\eta_{g0}^{I}, \eta_{g0}^{II}]$ were provided by Xu et al. (2019c) and are summarized in Table 4. The corresponding $\eta_{g0}^{\alpha\beta}$ are used in PFDD simulations.

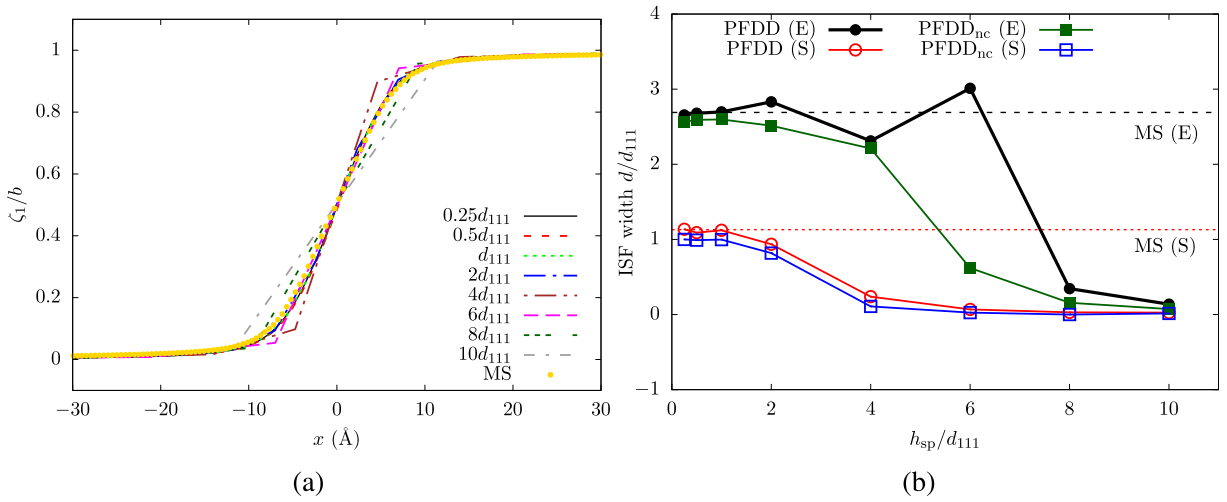

Fig. 15. (a) Disregistry fields of a screw monopole along the perfect dislocation Burgers vector direction, as a function of the grid spacing within the slip plane, $h_{sp} = h_x = h_z$. Results are based on PFDD$_{nc}$, with the grid spacing $h_y = d_{111}$ and the timestep size $\Delta t = 0.01$. (b) ISF widths, d, predicted by PFDD and PFDD$_{nc}$ simulations, for both edge (E) and screw (S) monopoles; the MS-based results are indicated by two horizontal dashed lines.

Table 3 and Fig. 12 show that, while PFDD and PFDD$_{ugc}$ predict the same ISF width for the same dislocation, the shape of the disregistry profile differs. Specifically, the PFDD model equipped with non-uniform $\eta_{g0}^{\alpha\beta}$ predicts dislocation core structures in better agreement with MS. We also find that, PFDD$_{ugc}$ predicts lower Peierls stresses than PFDD. Note that a dissociated dislocation with a larger ISF width (e.g., in Cu) is usually considered to have a lower Peierls stress than that with a smaller ISF width (e.g., in Al) (Liu et al., 2016, 2017a). While this is generally true, our calculations demonstrate that, in the same material, two dislocations having the same ISF width but different disregistry profiles may have different Peierls stresses. Our comparison highlights the sensitivity of the Peierls stress to the detailed dislocation core structure.

5.3. PFDD vs. PFDD$_{nc}$

Here, we assess the consequences of confining all slips to the slip plane in PFDD-based models, by comparing PFDD with PFDD$_{nc}$. First, we study the influences of the in-slip-plane grid spacing d_{sp} in PFDD$_{nc}$ and find them to be similar to those in PFDD, as shown in Fig. 15. It is also found that, for the same monopole and with the same grid spacings, PFDD$_{nc}$ predicts a smaller ISF width and a higher Peierls stress than PFDD. These results may be explained as follows. PFDD$_{nc}$ takes non-zero $\boldsymbol{\phi}(y \neq 0)$ into account, which effectively distributes the dislocation core to the whole system, leading to a less pronounced degree of slip within the slip plane. On the other hand, PFDD sets $\boldsymbol{\phi}(y \neq 0) = \mathbf{0}$, concentrating all slips to the slip plane and facilitating the dislocation dissociation, hence a larger ISF width and a lower Peierls stress.

5.4. PFDD vs. PFDD$_{iso}$

When the material is assumed elastic isotropic, the elastic stiffness tensor $\boldsymbol{C}_E$ becomes

$$\boldsymbol{C}_E^{iso} \equiv \begin{bmatrix} K+\frac{4}{3}\mu & & & & & \\ K-\frac{2}{3}\mu & K+\frac{4}{3}\mu & & & & \\ K-\frac{2}{3}\mu & K-\frac{2}{3}\mu & K+\frac{4}{3}\mu & & \text{Sym} & \\ & & & \mu & & \\ & & & & \mu & \\ & & & & & \mu \end{bmatrix}, \tag{26}$$

where K is the bulk modulus. Multiple isotropic averages have been developed to determine K and μ based on the independent elastic constants (Berge et al., 1993). Here, we use the isotropic average proposed by Hill (1952), which was shown to retain the same K as cubic elastic anisotropy (Szajewski et al., 2017), relevant to Al. In the Hill average (superscript H),

$$\boldsymbol{C}_E^H = \frac{1}{2}(\boldsymbol{C}_E^V + \boldsymbol{C}_E^R), \tag{27}$$

where superscripts V and R denote the isotropic Voigt (Voigt, 1889) and Reuss (Reuss, 1929) averages, respectively. In the Voigt average, the two independent constants in $\boldsymbol{C}_{\mathrm{E}}^{\mathrm{V}}$ are

$$\mu^{\mathrm{V}} = \frac{1}{15}[(C_{11}+C_{22}+C_{33})-(C_{12}+C_{23}+C_{13})+3(C_{44}+C_{55}+C_{66})], \tag{28}$$

$$K^{\mathrm{V}} = \frac{1}{9}[(C_{11}+C_{22}+C_{33})+2(C_{12}+C_{23}+C_{13})]. \tag{29}$$

In the Reuss average, the anisotropic elastic compliance tensor $\boldsymbol{S}_{\mathrm{E}}$ is first formed via $\boldsymbol{S}_{\mathrm{E}} = [\boldsymbol{C}_{\mathrm{E}}]^{-1}$, then the two independent constants in $\boldsymbol{C}_{\mathrm{E}}^{\mathrm{R}}$ are

$$\mu^{\mathrm{R}} = \frac{15}{4(S_{11}+S_{22}+S_{33})-4(S_{12}+S_{23}+S_{13})+3(S_{44}+S_{55}+S_{66})}, \tag{30}$$

$$K^{\mathrm{R}} = \frac{1}{(S_{11}+S_{22}+S_{33})+2(S_{12}+S_{23}+S_{13})}. \tag{31}$$

As shown in Table 3 and Fig. 12, compared with PFDD, $\mathrm{PFDD}_{\mathrm{iso}}$ predicts a smaller and larger ISF width d associated with the edge and screw monopoles, respectively. These findings agree with previous atomistic (Rasmussen et al., 1997), GPN (Szajewski et al., 2017), and PFDD simulations (Xu et al., 2019d). We note that the differences in d between PFDD and $\mathrm{PFDD}_{\mathrm{iso}}$ are relatively small: 0.4% and 4.4% for the edge and screw dipoles, respectively. The results are expected because Al is nearly elastically isotropic. The differences in the Peierls stress σ_{P}, however, are relatively large: 17% and 1.2% for the edge and screw monopoles, respectively. It is of note that $\mathrm{PFDD}_{\mathrm{iso}}$ predicts a larger σ_{P} than PFDD for both monopoles. This is different from the way in which the isotropic average alters d. Again, our results demonstrate that, knowledge of the ISF widths of two dislocations, even in the same material, is not sufficient in predicting which dislocation has a higher (or lower) Peierls stress.

6. Discussion

Our analyses in Sections 4 and 5 demonstrate the sensitivity of the predicted disregistry fields and Peierls stresses to time/grid resolution, simulation cell size, and detailed modeling choice. For the two in-slip-plane grid spacings in PFDD, we find that the one along the straight dislocation line, h_z, does not affect the results; for the other direction, larger grid spacings, h_x, generally result in smaller ISF width d. For convergence of the disregistry, the largest allowable h_x and the largest allowable timestep size Δt are, respectively, larger and smaller in PFDD than in $\mathrm{PFDD}_{\mathrm{ng}}$. This is in contrast to CAC, wherein larger finite elements in the coarse-grained domain yield larger d.

Neglecting ψ_{gra} or considering the non-zero order parameters within the non-slip-planes decreases d and increases σ_{P}. Treating the gradient energy coefficients $\eta_{\mathrm{g0}}^{\alpha\beta}$ as a uniform variable or non-uniform ones, naturally, lead to the same d, as long as the coefficients are fit to the same MS results. However, the calculated σ_{P} are different. Approximating Al, which is nearly elastically isotropic, as an isotropic medium overestimates and underestimates, respectively, d associated with a screw and an edge dislocation. The elastic isotropy-induced changes in σ_{P}, which are positive for both dislocations, are on average larger than those in d. Taken together, our results suggest that, even slight changes in the disregistry field can have relatively large influences on the Peierls stress.

Our simulations show that, for Al, it is recommended to (i) add ψ_{gra} to the total energy density, (ii) consider $\eta_{\mathrm{g0}}^{\alpha\beta}$ as independent variables and fit them to MS individually, (iii) confine all slips to pre-defined slip planes, and (iv) treat the material as an elastically anisotropic medium. Since Al has a relatively high ISF energy among FCC metals (Su et al., 2019a), it is useful to discuss the applicability of these four recommendations to other metals, e.g., those with a relatively low ISF energy. First, it is always desirable to adopt recommendations (iii) and (iv) because confining all slips to pre-defined slip planes and employing elastic anisotropy lead to a better representation of actual materials. Second, it may not be desirable, in some cases, to include ψ_{gra} in the total energy density, because doing so in PFDD may yield poorer results (with respect to MS) compared with $\mathrm{PFDD}_{\mathrm{ng}}$. The effects of ψ_{gra} depend on the complex relation between the elastic energy and GSFE (Xu et al., 2019d). Nevertheless, if one determines that ψ_{gra} should be included, it would always be desirable to consider $\eta_{\mathrm{g0}}^{\alpha\beta}$ as independent variables instead of a uniform one.

The ISF widths d and Peierls stresses σ_{P} reported here qualitatively agree with those in the literature in that d and σ_{P}, respectively, are larger and lower, for an edge monopole than for a screw monopole. It is tempting to compare results in this paper with others in the literature, based on either PF, GPN, SVPN, atomistics, or DFT. However, direct comparisons are not straightforward for several reasons. The first challenge lies in how the ISF width d is determined. While d is universally considered the distance between the center of two Shockley partial dislocation cores, a variety of approaches were employed in the literature to pinpoint the partial dislocation center. Our previous work (Xu et al., 2019b) showed that different methods to calculate d can lead to results that differ by up to a factor of 3.

Second, most existing PF, GPN, and SVPN simulations either were not informed by the same interatomic potential employed here or used parameterized functions for the GSFE surface, as opposed to direct calculations in this work.

Third, different types of atomistic calculations usually yield different Peierls stresses σ_{P}, even for the same dislocation using the same interatomic potential. For example, using the same EAM potential (Mishin et al., 1999) adopted in this paper, nudged elastic band (Tsuru et al., 2010) and direct MS calculations (Dang and Spearot, 2018), respectively, predict 1.84 MPa (edge) and 40.88 MPa (screw), and 1.34 MPa (edge) and 30.5 MPa (screw). The nudged elastic band method of Tsuru et al. (2010) should provide more accurate results. However, in their model, the top and bottom {111} atomic planes are constrained. This is analogous to an unrelaxed GSFE calculation leading to a higher energy barrier, thus a higher Peierls stress than that predicted by direct MS (Dang and Spearot,

2018). The simulation cell in the work of Dang and Spearot (2018) is loaded based on the deformation of boundary atoms. Thus, the system is not under pure shear stress state. Non-zero normal stress components and additional shear components will affect the Peierls stress. Using another interatomic potential (Mendelev et al., 2008) in MS, Cho et al. (2015) reported 5.46 MPa (edge) and 69.97 MPa (screw), while Dang and Spearot (2018) reported 6.36 MPa (edge) and 86.3 MPa (screw). The differences are likely due to the different ways in which the non-periodic boundaries in small-sized volumes are handled (Olmsted et al., 2001).

We remark that, PFDD models can be informed by DFT, an electronic structure calculation and more accurate than the MS method. This has been realized in a prior work (Xu et al., 2019d) but not here, because CAC is based on an interatomic potential. For comparability, then, all PFDD models in this work are informed by the same interatomic potential used in CAC and benchmarked against MS. On the other hand, most interatomic potentials, including the one used here, are fit to DFT data, so our simulations are based on DFT indirectly. It is worth noting that dislocation cores in Al have been modeled by DFT directly (Choly et al., 2005; Lu et al., 2006; Liu et al., 2007; Woodward et al., 2008; Shin et al., 2009; Shin and Carter, 2013; Iyer et al., 2015; Das and Gavini, 2017). In future PFDD work, the gradient energy coefficients may be fit to DFT-based disregistry fields, with all other parameters informed also by DFT (Juan and Kaxiras, 1996; Hartford et al., 1998; Lu et al., 2000a, 2001; Kamimura et al., 2018; Edagawa et al., 2019).

7. Conclusions

In this work, an extended dislocation in Al with pure edge or pure screw character is simulated using several models, including five PFDD variants and the CAC method. The PFDD variants differ in many aspects: (i) inclusion or exclusion of the gradient energy density, ψ_{gra}, (ii) uniform or non-uniform gradient energy coefficients, $\eta_{\text{g0}}^{\alpha\beta}$, (iii) confined or unconfined slip to the slip plane, and (iv) elastic isotropic or anisotropic. First, we conduct a systematic convergence study of the time/grid resolution and simulation cell size in these approaches. Then, we study the impact of different model parameters between PFDD variants on the predicted disregistry field and Peierls stress. MS simulations are carried out as a benchmark. It is found that

1. Varying the grid spacing along the dislocation line direction does not affect the PFDD-predicted disregistry, suggesting that, if a dislocation is known to remain straight, a large grid spacing may be applied along that direction without compromising the accuracy;
2. For PFDD results to be comparable with those from atomistics, grid spacings with atomic resolution should be applied within the plane that is normal to the dislocation line. As the grid spacings increase, the predicted dislocations become compact, i.e., the ISF width d approaches zero. Meanwhile, as the finite element size increases in CAC, d increases and the Peierls stress σ_{P} decreases;
3. For the same dislocation in PFDD, including ψ_{gra} and/or confining all slips to the slip plane increases d and decreases σ_{P};
4. Treating $\eta_{\text{g0}}^{\alpha\beta}$ as independent variables and fitting them to MS-based disregistry fields yield more accurate description of the dislocation core structures. Alternatively, using a uniform $\eta_{\text{g0}}^{\alpha\beta}$ that is fit to the same MS-based d results in different disregistry fields and σ_{P};
5. Approximating an elastic anisotropic medium as an isotropic one results in an overestimation and underestimation of d, respectively, associated with the screw and edge dislocations. Doing so also increases σ_{P} of both dislocations.

This paper focuses on comparing different continuum models in studying dislocations in an FCC metal. It would also be interesting to compare PFDD-, CAC-, and MS-based modeling of dislocations in metals with non-FCC lattices, e.g., body-centered cubic (BCC). Recently, PFDD (Peng et al., 2020) and CAC (Xu, 2018) were extended to the BCC lattice. The two models are termed "PFDD_{bcc}" and "CAC_{bcc}" here. Another PF dislocation model, the microscopic phase-field (MPF) model (Shen et al., 2014), was also recently extended to BCC systems (Qiu et al., 2019), which is termed "MPF_{bcc}" here. Similar to PFDD_{ng}, both PFDD_{bcc} and MPF_{bcc} exclude ψ_{gra} from the total energy density. In the meantime, three differences exist between the two models: (i) one and two order parameters are used per {110} slip plane, respectively, in PFDD_{bcc} and MPF_{bcc}; (ii) Eq. (4) is followed in MPF_{bcc} while a different energy density functional is used in PFDD_{bcc} to approximate the character angle dependence of the Peierls potential; and (iii) the slips are confined to slip planes in MPF_{bcc} but not in PFDD_{bcc}. As Qiu et al. (2019) pointed out, MPF_{bcc} cannot describe non-planar dislocations cores or high angle grain boundaries wherein dislocation cores are closely spaced or overlapping. The same can be said for PFDD_{bcc}. The localization of the slips to fault planes is also true for CAC_{bcc}. In addition to BCC metals, PFDD has also been extended to hexagonal close-packed (HCP) metals (Albrecht et al., 2020), while CAC has not. In this regard, further development in both PFDD and CAC methods for modeling dislocations in BCC and HCP systems are expected.

Declaration of competing interest

The authors declare that they have no known competing financial interests or personal relationships that could have appeared to influence the work reported in this paper.

CRediT authorship contribution statement

Shuozhi Xu: Conceptualization, Methodology, Software, Formal analysis, Resources, Data curation, Writing - original draft, Writing - review & editing, Visualization. **Jaber R. Mianroodi:** Conceptualization, Methodology, Software, Validation, Formal analysis, Writing - original draft, Writing - review & editing. **Abigail Hunter:** Conceptualization, Software, Writing - review & editing, Funding acquisition. **Bob Svendsen:** Conceptualization, Resources, Writing - original draft, Writing - review & editing, Supervision, Funding acquisition. **Irene J. Beyerlein:** Conceptualization, Resources, Writing - review & editing, Supervision, Funding acquisition.

Acknowledgments

We thank Dr. Youping Chen, Dr. Yang Xiang, and Ms. Lauren Smith for helpful discussions. The work of SX was supported in part by the Elings Prize Fellowship in Science offered by the California NanoSystems Institute (CNSI) on the UC Santa Barbara campus. SX and IJB gratefully acknowledge support in part from the Office of Naval Research under contract ONR BRC Grant N00014-18-1-2392. Use was made of computational facilities purchased with funds from the National Science Foundation (CNS-1725797) and administered by the Center for Scientific Computing (CSC). The CSC is supported by the CNSI and the Materials Research Science and Engineering Center (MRSEC; NSF DMR 1720256) at UC Santa Barbara. This work used the Extreme Science and Engineering Discovery Environment (XSEDE), which is supported by National Science Foundation grant number ACI-1053575. JRM and BS gratefully acknowledge partial support from the Deutsche Forschungsgemeinschaft (DFG) through Subproject M5 (M8) in the Priority Programme 1713. AH gratefully acknowledges support from the Materials project within the Physics and Engineering Models (PEM) Subprogram element of the Advanced Simulation and Computing (ASC) Program at Los Alamos National Laboratory (LANL), USA.

Appendix

Here, we show that, in PFDD$_{\rm nc}$, $\boldsymbol{\phi}$ may be non-zero on non-slip planes. Without loss of generality, we consider a simple model with only one order parameter ϕ_α within one slip plane, and

$$\boldsymbol{H}_{\rm R}(\phi_\alpha) = \frac{b_\alpha \phi_\alpha}{d_\alpha} \boldsymbol{s}_\alpha \otimes \boldsymbol{n}_\alpha \,, \tag{A.1}$$

$$\psi_{\rm gsf} = \frac{4\gamma^{\rm p}}{l_{\rm gsf}} \left[\frac{1}{4} - \left(\phi_\alpha - \frac{1}{2} \right)^2 \right] , \tag{A.2}$$

$$\psi_{\rm gra} = 0 \,, \tag{A.3}$$

where $\gamma^{\rm p}$ is the peak value of the GSFE curve.

It follows that

$$\psi(\boldsymbol{E}, \phi_\alpha) = \frac{1}{2} (\boldsymbol{E} - \phi_\alpha \boldsymbol{A}) \cdot \boldsymbol{C}_{\rm E} (\boldsymbol{E} - \phi_\alpha \boldsymbol{A}) + \frac{4\gamma^{\rm p}}{l_{\rm gsf}} \left[\frac{1}{4} - \left(\phi_\alpha - \frac{1}{2} \right)^2 \right] , \tag{A.4}$$

where

$$\boldsymbol{A} = {\rm sym} \frac{b_\alpha}{d_\alpha} \boldsymbol{s}_\alpha \otimes \boldsymbol{n}_\alpha \,. \tag{A.5}$$

According to Eq. (12), $\dot{\phi}_\alpha = 0$ when $\partial_{\phi_\alpha} \psi = 0$, i.e.,

$$\partial_{\phi_\alpha} \psi = \frac{1}{2} \left[(\partial_{\phi_\alpha} \boldsymbol{E} - \boldsymbol{A}) \cdot \boldsymbol{C}_{\rm E} (\boldsymbol{E} - \phi_\alpha \boldsymbol{A}) + (\boldsymbol{E} - \phi_\alpha \boldsymbol{A}) \cdot \boldsymbol{C}_{\rm E} (\partial_{\phi_\alpha} \boldsymbol{E} - \boldsymbol{A}) \right] - \frac{8\gamma^{\rm p} \phi_\alpha - 4\gamma^{\rm p}}{l_{\rm gsf}} = 0 \,. \tag{A.6}$$

Note that $\partial_{\phi_\alpha} \boldsymbol{E} = \boldsymbol{0}$, so

$$\phi_\alpha \boldsymbol{A} \cdot \boldsymbol{C}_{\rm E} \boldsymbol{A} - \frac{8\gamma^{\rm p} \phi_\alpha}{l_{\rm gsf}} - \frac{1}{2} (\boldsymbol{A} \cdot \boldsymbol{C}_{\rm E} \boldsymbol{E} + \boldsymbol{E} \cdot \boldsymbol{C}_{\rm E} \boldsymbol{A}) + \frac{4\gamma^{\rm p}}{l_{\rm gsf}} = 0 \,. \tag{A.7}$$

Then

$$\phi_\alpha = \frac{\frac{1}{2} (\boldsymbol{A} \cdot \boldsymbol{C}_{\rm E} \boldsymbol{E} + \boldsymbol{E} \cdot \boldsymbol{C}_{\rm E} \boldsymbol{A}) - \frac{4\gamma^{\rm p}}{l_{\rm gsf}}}{\boldsymbol{A} \cdot \boldsymbol{C}_{\rm E} \boldsymbol{A} - \frac{8\gamma^{\rm p}}{l_{\rm gsf}}} \,, \tag{A.8}$$

where all quantities, except $\boldsymbol{E}$, are constants over the entire domain. Therefore, $\phi_\alpha \neq 0$ at most, if not all, continuum points.

References

Albrecht, C., Hunter, A., Kumar, A., Beyerlein, I., 2020. A phase field model for dislocations in hexagonal close packed crystals. J. Mech. Phys. Solids 137, http://dx.doi.org/10.1016/j.jmps.2019.103823, URL https://www.sciencedirect.com/science/article/pii/S0022509619306751.

Allen, S.M., Cahn, J.W., 1979. A macroscopic theory for antiphase boundary motion and its application to antiphase domain coarsening. Acta Metall. 27, 1085–1095.

Berge, P.A., Berryman, J.G., Bonner, B.P., 1993. Influence of microstructure on rock elastic properties. Geophys. Res. Lett. 20 (23), 2619–2622. http://dx.doi.org/10.1029/93GL03131, URL https://agupubs.onlinelibrary.wiley.com/doi/abs/10.1029/93GL03131.

Bitzek, E., Koskinen, P., Gähler, F., Moseler, M., Gumbsch, P., 2006. Structural relaxation made simple. Phys. Rev. Lett. 97 (17), 170201. http://dx.doi.org/10.1103/PhysRevLett.97.170201, URL http://link.aps.org/doi/10.1103/PhysRevLett.97.170201.

Bulatov, V., Cai, W., 2006. Computer Simulations of Dislocations. Oxford University Press, Oxford ; New York.

Bulatov, V.V., Kaxiras, E., 1997. Semidiscrete variational Peierls framework for dislocation core properties. Phys. Rev. Lett. 78 (22), 4221–4224. http://dx.doi.org/10.1103/PhysRevLett.78.4221, URL https://link.aps.org/doi/10.1103/PhysRevLett.78.4221.

Cahn, J.W., Hilliard, J.E., 1958. Free energy of a non-uniform system. I. Interfacial energy. J. Chem. Phys. 28, 258–267.

Chavoshi, S.Z., Xu, S., 2019. Nanoindentation/scratching at finite temperatures: Insights from atomistic-based modeling. Prog. Mater. Sci. 100, 1–20. http://dx.doi.org/10.1016/j.pmatsci.2018.09.002, URL http://www.sciencedirect.com/science/article/pii/S0079642518300914.

Chen, Y., 2006. Local stress and heat flux in atomistic systems involving three-body forces. J. Chem. Phys. 124 (5), 054113. http://dx.doi.org/10.1063/1.2166387, URL http://scitation.aip.org/content/aip/journal/jcp/124/5/10.1063/1.2166387.

Chen, Y., 2009. Reformulation of microscopic balance equations for multiscale materials modeling. J. Chem. Phys. 130 (13), 134706. http://dx.doi.org/10.1063/1.3103887, URL http://jcp.aip.org/resource/1/jcpsa6/v130/i13/p134706_s1.

Chen, Y., Lee, J., 2005. Atomistic formulation of a multiscale field theory for nano/micro solids. Phil. Mag. 85 (33–35), 4095–4126. http://dx.doi.org/10.1080/14786430500362595, URL http://www.tandfonline.com/doi/abs/10.1080/14786430500362595.

Chen, H., Xu, S., Li, W., Ji, R., Phan, T., Xiong, L., 2018. A spatial decomposition parallel algorithm for a concurrent atomistic-continuum simulator and its preliminary applications. Comput. Mater. Sci. 144, 1–10. http://dx.doi.org/10.1016/j.commatsci.2017.11.051, URL https://www.sciencedirect.com/science/article/pii/S0927025617306845.

Chen, Y., Zimmerman, J., Krivtsov, A., McDowell, D.L., 2011. Assessment of atomistic coarse-graining methods. Inter. J. Eng. Sci. 49 (12), 1337–1349. http://dx.doi.org/10.1016/j.ijengsci.2011.03.018, URL http://www.sciencedirect.com/science/article/pii/S0020722511000747.

Cho, J., Junge, T., Molinari, J.-F., Anciaux, G., 2015. Toward a 3D coupled atomistic and discrete dislocation dynamics simulation: dislocation core structures and peierls stresses with several character angles in FCC aluminum. Adv. Model. Simul. Eng. Sci. 2 (1), 12. http://dx.doi.org/10.1186/s40323-015-0028-6, URL http://www.amses-journal.com/content/2/1/12/abstract.

Choly, N., Lu, G., E, W., Kaxiras, E., 2005. Multiscale simulations in simple metals: A density-functional-based methodology. Phys. Rev. B 71 (9), 094101. http://dx.doi.org/10.1103/PhysRevB.71.094101, URL https://link.aps.org/doi/10.1103/PhysRevB.71.094101.

Cottrell, A.H., 2002. Commentary. A brief view of work hardening. In: Duesbery, M.S., Nabarro, F.R.N. (Eds.), Dislocations in Solids, Vol. 11. Elsevier, pp. vii–xvii, URL http://www.sciencedirect.com/science/article/pii/S157248590280002X.

Dang, K., Spearot, D., 2018. Pressure dependence of the Peierls stress in aluminum. JOM 70 (7), 1094–1099. http://dx.doi.org/10.1007/s11837-018-2819-y.

Das, S., Gavini, V., 2017. Electronic structure study of screw dislocation core energetics in Aluminum and core energetics informed forces in a dislocation aggregate. J. Mech. Phys. Solids 104, 115–143. http://dx.doi.org/10.1016/j.jmps.2017.03.010, URL http://www.sciencedirect.com/science/article/pii/S0022509617300820.

Edagawa, K., Kamimura, Y., Iskandarov, A.M., Umeno, Y., Takeuchi, S., 2019. Peierls stresses estimated by a discretized Peierls-Nabarro model for a variety of crystals. Materialia 5, 100218. http://dx.doi.org/10.1016/j.mtla.2019.100218, URL http://www.sciencedirect.com/science/article/pii/S2589152919300134.

Eringen, A.C. (Ed.), 2004. Nonlocal Continuum Field Theories, first ed. Springer, New York, NY, URL http://link.springer.com/10.1007/b97697.

Gunter, D., Kaper, H., Leaf, G., 2002. Implicit integration of the time-dependent Ginzburg-Landau equations of superconductivity. SIAM J. Sci. Comput. 23 (6), 1943–1958. http://dx.doi.org/10.1137/S1064827500375473, URL https://epubs.siam.org/doi/10.1137/S1064827500375473.

Hale, L.M., 2018. Comparing modeling predictions of aluminum edge dislocations: Semidiscrete variational Peierls-Nabarro versus atomistics. JOM 70 (7), 1100–1105. http://dx.doi.org/10.1007/s11837-018-2836-x.

Hartford, J., von Sydow, B., Wahnstrm, G., Lundqvist, B.I., 1998. Peierls barriers and stresses for edge dislocations in Pd and Al calculated from first principles. Phys. Rev. B 58 (5), 2487–2496. http://dx.doi.org/10.1103/PhysRevB.58.2487, URL https://link.aps.org/doi/10.1103/PhysRevB.58.2487.

Hill, R., 1952. The elastic behaviour of a crystalline aggregate. Proc. Phys. Soc. A 65 (5), 349–354. http://dx.doi.org/10.1088/0370-1298/65/5/307.

Hohenberg, P.C., Halperin, B.I., 1977. Theory of dynamic critical phenomena. Rev. Modern Phys. 49, 435–479.

Hu, S.Y., Li, Y.L., Zheng, Y.X., Chen, L.Q., 2004. Effect of solutes on dislocation motion — a phase-field simulation. Int. J. Plast. 20 (3), 403–425. http://dx.doi.org/10.1016/S0749-6419(03)00094-9, URL http://www.sciencedirect.com/science/article/pii/S0749641903000949.

Iyer, M., Radhakrishnan, B., Gavini, V., 2015. Electronic-structure study of an edge dislocation in Aluminum and the role of macroscopic deformations on its energetics. J. Mech. Phys. Solids 76, 260–275. http://dx.doi.org/10.1016/j.jmps.2014.12.009, URL http://www.sciencedirect.com/science/article/pii/S002250961400249X.

Joós, B., Duesbery, M.S., 1997. The Peierls stress of dislocations: An analytic formula. Phys. Rev. Lett. 78 (2), 266–269. http://dx.doi.org/10.1103/PhysRevLett.78.266, URL https://link.aps.org/doi/10.1103/PhysRevLett.78.266.

Joós, B., Ren, Q., Duesbery, M.S., 1994. Peierls-Nabarro model of dislocations in silicon with generalized stacking-fault restoring forces. Phys. Rev. B 50 (9), 5890–5898. http://dx.doi.org/10.1103/PhysRevB.50.5890, URL https://link.aps.org/doi/10.1103/PhysRevB.50.5890.

Juan, Y.-M., Kaxiras, E., 1996. Generalized stacking fault energy surfaces and dislocation properties of silicon: A first-principles theoretical study. Phil. Mag. A 74 (6), 1367–1384. http://dx.doi.org/10.1080/01418619608240729.

Kamimura, Y., Edagawa, K., Iskandarov, A.M., Osawa, M., Umeno, Y., Takeuchi, S., 2018. Peierls stresses estimated via the Peierls-Nabarro model using *ab-initio* γ-surface and their comparison with experiments. Acta Mater. 148, 355–362. http://dx.doi.org/10.1016/j.actamat.2018.02.009, URL http://www.sciencedirect.com/science/article/pii/S1359645418301101.

Koslowski, M., Cuitio, A.M., Ortiz, M., 2002. A phase-field theory of dislocation dynamics, strain hardening and hysteresis in ductile single crystals. J. Mech. Phys. Solids 50 (12), 2597–2635. http://dx.doi.org/10.1016/S0022-5096(02)00037-6, URL http://www.sciencedirect.com/science/article/pii/S0022509602000376.

Levitas, V.I., 2018. Phase field approach for stress- and temperature-induced phase transformations that satisfies lattice instability conditions. Part I. General theory. Int. J. Plast. 106, 164–185. http://dx.doi.org/10.1016/j.ijplas.2018.03.007, URL http://www.sciencedirect.com/science/article/pii/S0749641918300056.

Liu, G., Cheng, X., Wang, J., Chen, K., Shen, Y., 2016. Peierls stress in face-centered-cubic metals predicted from an improved semi-discrete variation Peierls-Nabarro model. Scr. Mater. 120, 94–97. http://dx.doi.org/10.1016/j.scriptamat.2016.04.013, URL http://www.sciencedirect.com/science/article/pii/S1359646216301348.

Liu, G., Cheng, X., Wang, J., Chen, K., Shen, Y., 2017a. Atomically informed nonlocal semi-discrete variational Peierls-Nabarro model for planar core dislocations. Sci. Rep. 7, 43785. http://dx.doi.org/10.1038/srep43785, URL https://www.nature.com/articles/srep43785.

Liu, G., Cheng, X., Wang, J., Chen, K., Shen, Y., 2017b. Quasi-periodic variation of Peierls stress of dislocations in face-centered-cubic metals. Int. J. Plast. 90, 156–166. http://dx.doi.org/10.1016/j.ijplas.2017.01.002, URL http://www.sciencedirect.com/science/article/pii/S074964191730027X.

Liu, Y., Lu, G., Chen, Z., Kioussis, N., 2007. An improved QM/MM approach for metals. Modelling Simul. Mater. Sci. Eng. 15 (3), 275. http://dx.doi.org/10.1088/0965-0393/15/3/006, URL http://stacks.iop.org/0965-0393/15/i=3/a=006.

Lu, G., Kioussis, N., Bulatov, V.V., Kaxiras, E., 2000a. Generalized-stacking-fault energy surface and dislocation properties of aluminum. Phys. Rev. B 62 (5), 3099–3108. http://dx.doi.org/10.1103/PhysRevB.62.3099, URL https://link.aps.org/doi/10.1103/PhysRevB.62.3099.

Lu, G., Kioussis, N., Bulatov, V.V., Kaxiras, E., 2000b. The Peierls-Nabarro model revisited. Phil. Mag. 80 (10), 675–682. http://dx.doi.org/10.1080/09500830050143778, URL https://doi.org/10.1080/09500830050143778.

Lu, G., Kioussis, N., Bulatov, V.V., Kaxiras, E., 2001. Dislocation core properties of aluminum: a first-principles study. Mater. Sci. Eng.: A 309–310, 142–147. http://dx.doi.org/10.1016/S0921-5093(00)01711-1, URL http://www.sciencedirect.com/science/article/pii/S0921509300017111.

Lu, G., Tadmor, E.B., Kaxiras, E., 2006. From electrons to finite elements: A concurrent multiscale approach for metals. Phys. Rev. B 73 (2), 024108. http://dx.doi.org/10.1103/PhysRevB.73.024108, URL https://link.aps.org/doi/10.1103/PhysRevB.73.024108.

Mendelev, M.I., Kramer, M.J., Becker, C.A., Asta, M., 2008. Analysis of semi-empirical interatomic potentials appropriate for simulation of crystalline and liquid Al and Cu. Phil. Mag. 88 (12), 1723–1750. http://dx.doi.org/10.1080/14786430802206482.

Mianroodi, J.R., Hunter, A., Beyerlein, I., Svendsen, B., 2016. Theoretical and computational comparison of models for dislocation dissociation and stacking fault / core formation in fcc crystals. J. Mech. Phys. Solids 95, 719–741.

Mianroodi, J.R., Svendsen, B., 2015. Atomistically determined phase field modeling of dislocation dissociation, stacking fault formation, dislocation slip, and reactions in fcc systems. J. Mech. Phys. Solids 77, 109–122.

Miller, R., Phillips, R., Beltz, G., Ortiz, M., 1998. A non-local formulation of the peierls dislocation model. J. Mech. Phys. Solids 46 (10), 1845–1867. http://dx.doi.org/10.1016/S0022-5096(98)00057-X, URL http://www.sciencedirect.com/science/article/pii/S002250969800057X.

Mishin, Y., Farkas, D., Mehl, M.J., Papaconstantopoulos, D.A., 1999. Interatomic potentials for monoatomic metals from experimental data and *ab initio* calculations. Phys. Rev. B 59 (5), 3393–3407. http://dx.doi.org/10.1103/PhysRevB.59.3393, URL http://link.aps.org/doi/10.1103/PhysRevB.59.3393.

Nabarro, F.R.N., 1947. Dislocations in a simple cubic lattice. Proc. Phys. Soc. 59 (2), 256. http://dx.doi.org/10.1088/0959-5309/59/2/309, URL http://stacks.iop.org/0959-5309/59/i=2/a=309.

Olmsted, D.L., Hardikar, K.Y., Phillips, R., 2001. Lattice resistance and Peierls stress in finite size atomistic dislocation simulations. Model. Simul. Mater. Sci. Eng. 9 (3), 215. http://dx.doi.org/10.1088/0965-0393/9/3/308, URL http://iopscience.iop.org/0965-0393/9/3/308.

Parrinello, M., Rahman, A., 1981. Polymorphic transitions in single crystals: A new molecular dynamics method. J. Appl. Phys. 52 (12), 7182–7190. http://dx.doi.org/10.1063/1.328693, URL http://scitation.aip.org/content/aip/journal/jap/52/12/10.1063/1.328693.

Peierls, R., 1940. The size of a dislocation. Proc. Phys. Soc. 52 (1), 34. http://dx.doi.org/10.1088/0959-5309/52/1/305, URL http://stacks.iop.org/0959-5309/52/i=1/a=305.

Peng, X., Mathew, N., Beyerlein, I.J., Dayal, K., Hunter, A., 2020. A 3D phase field dislocation dynamics model for body-centered cubic crystals. Comput. Mater. Sci. 171, 109217. http://dx.doi.org/10.1016/j.commatsci.2019.109217, URL http://www.sciencedirect.com/science/article/pii/S0927025619305166.

Plimpton, S., 1995. Fast parallel algorithms for short-range molecular dynamics. J. Comput. Phys. 117 (1), 1–19. http://dx.doi.org/10.1006/jcph.1995.1039, URL http://www.sciencedirect.com/science/article/pii/S002199918571039X.

Provatas, N., Elder, K., 2010. Phase Field Methods in Material Science and Engineering. Wiley-VCH, New York.

Qiu, D., Zhao, P., Shen, C., Lu, W., Zhang, D., Mrovec, M., Wang, Y., 2019. Predicting grain boundary structure and energy in BCC metals by integrated atomistic and phase-field modeling. Acta Mater. 164, 799–809. http://dx.doi.org/10.1016/j.actamat.2018.11.023, URL http://www.sciencedirect.com/science/article/pii/S1359645418308991.

Rasmussen, T., Jacobsen, K.W., Leffers, T., Pedersen, O.B., 1997. Simulations of the atomic structure, energetics, and cross slip of screw dislocations in copper. Phys. Rev. B 56 (6), 2977–2990. http://dx.doi.org/10.1103/PhysRevB.56.2977, URL https://link.aps.org/doi/10.1103/PhysRevB.56.2977.

Reuss, A., 1929. Berechnung der Fließgrenze von Mischkristallen auf Grund der Plastizitätsbedingung für Einkristalle. Z. Angew. Math. Mech. 9 (1), 49–58. http://dx.doi.org/10.1002/zamm.19290090104, URL https://onlinelibrary.wiley.com/doi/abs/10.1002/zamm.19290090104.

Rhee, M., Zbib, H.M., Hirth, J.P., Huang, H., Rubia, T.d.l., 1998. Models for long-/short-range interactions and cross slip in 3D dislocation simulation of BCC single crystals. Model. Simul. Mater. Sci. Eng. 6 (4), 467. http://dx.doi.org/10.1088/0965-0393/6/4/012, URL http://iopscience.iop.org/0965-0393/6/4/012.

Ruffini, A., Le Bouar, Y., Finel, A., 2017. Three-dimensional phase-field model of dislocations for a heterogeneous face-centered cubic crystal. J. Mech. Phys. Solids 105, 95–115. http://dx.doi.org/10.1016/j.jmps.2017.04.008, URL http://www.sciencedirect.com/science/article/pii/S0022509617302740.

Schoeck, G., 1994. The generalized Peierls-Nabarro model. Phil. Mag. A 69 (6), 1085–1095. http://dx.doi.org/10.1080/01418619408242240.

Schoeck, G., 1999. Peierls energy of dislocations: A critical assessment. Phys. Rev. Lett. 82 (11), 2310–2313. http://dx.doi.org/10.1103/PhysRevLett.82.2310, URL https://link.aps.org/doi/10.1103/PhysRevLett.82.2310.

Seol, D.J., Hu, S.Y., Li, Y.L., Shen, J., Oh, K.H., Chen, L.Q., 2003. Computer simulation of spinodal decomposition in constrained films. Acta Mater. 51 (17), 5173–5185. http://dx.doi.org/10.1016/S1359-6454(03)00378-1, URL http://www.sciencedirect.com/science/article/pii/S1359645403003781.

Shanthraj, P., Sharma, L., Svendsen, B., Roters, F., Raabe, D., 2016. A phase field model for damage in elasto-viscoplastic materials. Comput. Methods Appl. Mech. Engrg. 312, 167–185.

Shanthraj, P., Svendsen, B., Sharma, L., Roters, F., Raabe, D., 2017. Elasto-viscoplastic phase field modelling of anisotropic cleavage fracture. J. Mech. Phys. Solids 99, 19–34.

Shen, C., Li, J., Wang, Y., 2014. Predicting structure and energy of dislocations and grain boundaries. Acta Mater. 74, 125–131. http://dx.doi.org/10.1016/j.actamat.2014.03.065, URL http://www.sciencedirect.com/science/article/pii/S135964541400233X.

Shen, C., Wang, Y., 2003. Phase field model of dislocation networks. Acta Mater. 51 (9), 2595–2610. http://dx.doi.org/10.1016/S1359-6454(03)00058-2, URL http://www.sciencedirect.com/science/article/pii/S1359645403000582.

Shin, I., Carter, E.A., 2013. Possible origin of the discrepancy in Peierls stresses of fcc metals: first-principles simulations of dislocation mobility in aluminum. Phys. Rev. B 88 (6), 064106. http://dx.doi.org/10.1103/PhysRevB.88.064106, URL https://link.aps.org/doi/10.1103/PhysRevB.88.064106.

Shin, I., Ramasubramaniam, A., Huang, C., Hung, L., Carter, E.A., 2009. Orbital-free density functional theory simulations of dislocations in aluminum. Phil. Mag. 89 (34–36), 3195–3213. http://dx.doi.org/10.1080/14786430903246353.

Su, Y., Xu, S., Beyerlein, I.J., 2019a. Density functional theory calculations of generalized stacking fault energy surfaces for eight face-centered cubic transition metals. J. Appl. Phys. 126 (10), 105112. http://dx.doi.org/10.1063/1.5115282, URL https://aip.scitation.org/doi/10.1063/1.5115282.

Su, Y., Xu, S., Beyerlein, I.J., 2019b. Ab initio-informed phase-field modeling of dislocation core structures in equal-molar CoNiRu multi-principal element alloys. Model. Simul. Mater. Sci. Eng. 27 (8), 084001. http://dx.doi.org/10.1088/1361-651X/ab3b62.

Szajewski, B.A., Hunter, A., Luscher, D.J., Beyerlein, I.J., 2017. The influence of anisotropy on the core structure of Shockley partial dislocations within FCC materials. Model. Simul. Mater. Sci. Eng. 26 (1), 015010. http://dx.doi.org/10.1088/1361-651X/aa9758.

Tsuru, T., Kaji, Y., Shibutani, Y., 2010. Minimum energy motion and core structure of pure edge and screw dislocations in Al. J. Comput. Sci. Tech. 4 (3), 185–193. http://dx.doi.org/10.1299/jcst.4.185, URL https://www.jstage.jst.go.jp/article/jcst/4/3/4_3_185/_article.

Voigt, W., 1889. Ueber die Beziehung zwischen den beiden Elasticitätsconstanten isotroper Körper. Ann. Phys. 274 (12), 573–587. http://dx.doi.org/10.1002/andp.18892741206, URL https://onlinelibrary.wiley.com/doi/abs/10.1002/andp.18892741206.

Wang, Y.U., Jin, Y.M., Cuitiño, A.M., Khachaturyan, A.G., 2001. Nanoscale phase field microelasticity theory of dislocations: model and 3D simulations. Acta Mater. 49 (10), 1847–1857. http://dx.doi.org/10.1016/S1359-6454(01)00075-1, URL http://www.sciencedirect.com/science/article/pii/S1359645401000751.

Wang, Y., Li, J., 2010. Phase field modeling of defects and deformation. Acta Mater. 58 (4), 1212–1235. http://dx.doi.org/10.1016/j.actamat.2009.10.041, URL http://www.sciencedirect.com/science/article/pii/S1359645409007447.

Warren, J.A., Kobayashi, R., Lobkovsky, A.E., Craig Carter, W., 2003. Extending phase field models of solidification to polycrystalline materials. Acta Mater. 51 (20), 6035–6058. http://dx.doi.org/10.1016/S1359-6454(03)00388-4, URL http://www.sciencedirect.com/science/article/pii/S1359645403003884.

Wei, H., Xiang, Y., Ming, P., 2008. A generalized Peierls-Nabarro model for curved dislocations using discrete Fourier transform. Comm. Comput. Phys. 4 (2), 275–293, URL http://www.global-sci.com/intro/article_detail/cicp/7790.html.

Woodward, C., Trinkle, D.R., Hector, L.G., Olmsted, D.L., 2008. Prediction of dislocation cores in aluminum from density functional theory. Phys. Rev. Lett. 100 (4), 045507. http://dx.doi.org/10.1103/PhysRevLett.100.045507, URL http://link.aps.org/doi/10.1103/PhysRevLett.100.045507.

Xiang, Y., 2006. Modeling dislocations at different scales. Comm. Comput. Phys. 1 (3), 383–424, URL http://www.global-sci.com/intro/article_detail/cicp/7962.html.

Xiang, Y., Wei, H., Ming, P., E, W., 2008. A generalized Peirls-Nabarro model for curved dislocations and core structures of dislocation loops in Al and Cu. Acta Mater. 56, 1447–1460.

Xiong, L., Rigelesaiyin, J., Chen, X., Xu, S., McDowell, D.L., Chen, Y., 2016. Coarse-grained elastodynamics of fast moving dislocations. Acta Mater. 104, 143–155. http://dx.doi.org/10.1016/j.actamat.2015.11.037, URL http://www.sciencedirect.com/science/article/pii/S1359645415300884.

Xiong, L., Tucker, G., McDowell, D.L., Chen, Y., 2011. Coarse-grained atomistic simulation of dislocations. J. Mech. Phys. Solids 59 (2), 160–177. http://dx.doi.org/10.1016/j.jmps.2010.11.005, URL http://www.sciencedirect.com/science/article/pii/S0022509610002395.

Xiong, L., Xu, S., McDowell, D.L., Chen, Y., 2015. Concurrent atomistic-continuum simulations of dislocation-void interactions in fcc crystals. Int. J. Plast. 65, 33–42. http://dx.doi.org/10.1016/j.ijplas.2014.08.002, URL http://www.sciencedirect.com/science/article/pii/S0749641914001508.

Xu, S., 2018. Modelling plastic deformation of nano/submicron-sized tungsten pillars under compression: A coarse-grained atomistic approach. Int. J. Multiscale Comput. Eng. 16 (4), 367–376. http://dx.doi.org/10.1615/IntJMultCompEng.2018026027, URL http://www.dl.begellhouse.com/journals/61fd1b191cf7e96f,77bb56c9113fd8ad,519a0e1634b8eddd.html.

Xu, S., Che, R., Xiong, L., Chen, Y., McDowell, D.L., 2015. A quasistatic implementation of the concurrent atomistic-continuum method for FCC crystals. Int. J. Plast. 72, 91–126. http://dx.doi.org/10.1016/j.ijplas.2015.05.007, URL http://www.sciencedirect.com/science/article/pii/S0749641915000777.

Xu, S., Chen, X., 2019. Modeling dislocations and heat conduction in crystalline materials: atomistic/continuum coupling approaches. Int. Mater. Rev. 64 (7), 407–438. http://dx.doi.org/10.1080/09506608.2018.1486358.

Xu, S., Chu, K., 2017. PyCAC User's Manual. http://www.pycac.org/ (Accessed: January 18, 2020).

Xu, S., Latypov, M.I., Su, Y., 2018a. Concurrent atomistic-continuum simulations of uniaxial compression of gold nano/submicropillars. Phil. Mag. Lett. 98 (5), 173–182. http://dx.doi.org/10.1080/09500839.2018.1515506.

Xu, S., McDowell, D.L., Beyerlein, I.J., 2019a. Sequential obstacle interactions with dislocations in a planar array. Acta Mater. 174, 160–172. http://dx.doi.org/10.1016/j.actamat.2019.05.030, URL http://www.sciencedirect.com/science/article/pii/S135964541930312X.

Xu, S., Mianroodi, J.R., Hunter, A., Beyerlein, I.J., Svendsen, B., 2019b. Phase-field-based calculations of the disregistry fields of static extended dislocations in FCC metals. Phil. Mag. 99 (11), 1400–1428. http://dx.doi.org/10.1080/14786435.2019.1582850.

Xu, S., Payne, T.G., Chen, H., Liu, Y., Xiong, L., Chen, Y., McDowell, D.L., 2018b. PyCAC: The concurrent atomistic-continuum simulation environment. J. Mater. Res. 33 (7), 857–871. http://dx.doi.org/10.1557/jmr.2018.8, URL https://www.cambridge.org/core/journals/journal-of-materials-research/article/pycac-the-concurrent-atomisticcontinuum-simulation-environment/E664F7A8C0AD8DD1673BE2BDE592D0AA.

Xu, S., Rigelesaiyin, J., Xiong, L., Chen, Y., McDowell, D.L., 2018c. Generalized continua concepts in coarse-graining atomistic simulations. In: Generalized Models and Non-Classical Approaches in Complex Materials 2. In: Advanced Structured Materials, Springer, Cham, pp. 237–260. http://dx.doi.org/10.1007/978-3-319-77504-3_12, URL https://link.springer.com/chapter/10.1007/978-3-319-77504-3_12.

Xu, S., Smith, L., Mianroodi, J.R., Hunter, A., Svendsen, B., Beyerlein, I.J., 2019c. A comparison of different continuum approaches in modeling mixed-type dislocations in Al. Model. Simul. Mater. Sci. Eng. 27 (7), 074004. http://dx.doi.org/10.1088/1361-651X/ab2d16.

Xu, S., Su, Y., Beyerlein, I.J., 2019d. Modeling dislocations with arbitrary character angle in face-centered cubic transition metals using the phase-field dislocation dynamics method with full anisotropic elasticity. Mech. Mater. 139, 103200. http://dx.doi.org/10.1016/j.mechmat.2019.103200, URL http://www.sciencedirect.com/science/article/pii/S0167663619303734.

Xu, S., Xiong, L., Chen, Y., McDowell, D.L., 2016a. An analysis of key characteristics of the Frank-Read source process in FCC metals. J. Mech. Phys. Solids 96, 460–476. http://dx.doi.org/10.1016/j.jmps.2016.08.002, URL http://www.sciencedirect.com/science/article/pii/S0022509616301016.

Xu, S., Xiong, L., Chen, Y., McDowell, D.L., 2016b. Edge dislocations bowing out from a row of collinear obstacles in Al. Scripta Mater. 123, 135–139. http://dx.doi.org/10.1016/j.scriptamat.2016.06.018, URL http://www.sciencedirect.com/science/article/pii/S135964621630272X.

Xu, S., Xiong, L., Chen, Y., McDowell, D.L., 2016c. Sequential slip transfer of mixed-character dislocations across Σ3 coherent twin boundary in FCC metals: a concurrent atomistic-continuum study. npj Comput. Mater. 2, 15016. http://dx.doi.org/10.1038/npjcompumats.2015.16, URL http://www.nature.com/articles/npjcompumats201516.

Xu, S., Xiong, L., Chen, Y., McDowell, D.L., 2017a. Comparing EAM potentials to model slip transfer of sequential mixed character dislocations across two symmetric tilt grain boundaries in Ni. JOM 69 (5), 814–821. http://dx.doi.org/10.1007/s11837-017-2302-1, URL https://link.springer.com/article/10.1007/s11837-017-2302-1.

Xu, S., Xiong, L., Chen, Y., McDowell, D.L., 2017b. Shear stress- and line length-dependent screw dislocation cross-slip in FCC Ni. Acta Mater. 122, 412–419. http://dx.doi.org/10.1016/j.actamat.2016.10.005, URL http://www.sciencedirect.com/science/article/pii/S1359645416307601.

Xu, S., Xiong, L., Chen, Y., McDowell, D.L., 2017c. Validation of the concurrent atomistic-continuum method on screw dislocation/stacking fault interactions. Crystals 7 (5), 120. http://dx.doi.org/10.3390/cryst7050120, URL http://www.mdpi.com/2073-4352/7/5/120.

Xu, S., Xiong, L., Deng, Q., McDowell, D.L., 2016d. Mesh refinement schemes for the concurrent atomistic-continuum method. Int. J. Solids Struct. 90, 144–152. http://dx.doi.org/10.1016/j.ijsolstr.2016.03.030, URL http://www.sciencedirect.com/science/article/pii/S0020768316300154.

Zhang, S.H., Beyerlein, I.J., Legut, D., Fu, Z.H., Zhang, Z., Shang, S.L., Liu, Z.K., Germann, T.C., Zhang, R.F., 2017. First-principles investigation of strain effects on the stacking fault energies, dislocation core structure, and Peierls stress of magnesium and its alloys. Phys. Rev. B 95 (22), 224106. http://dx.doi.org/10.1103/PhysRevB.95.224106, URL https://link.aps.org/doi/10.1103/PhysRevB.95.224106.

Zhang, S.H., Legut, D., Zhang, R.F., 2019. PNADIS: An automated Peierls Nabarro analyzer for dislocation core structure and slip resistance. Comput. Phys. Comm. 240, 60–73. http://dx.doi.org/10.1016/j.cpc.2019.03.005, URL http://www.sciencedirect.com/science/article/pii/S0010465519300839.

Zhu, A., Jin, C., Zhao, D., Xiang, Y., Huang, J., 2015. A numerical scheme for generalized Peierls-Nabarro model of dislocations based on the fast multipole method and iterative grid redistribution. Comm. Comput. Phys. 18 (5), 1282–1312. http://dx.doi.org/10.4208/cicp.130114.270315a, URL https://www.cambridge.org/core/journals/communications-in-computational-physics/article/numerical-scheme-for-generalized-peierlsnabarro-model-of-dislocations-based-on-the-fast-multipole-method-and-iterative-grid-redistribution/23F8204D31924663320E35988EE4647C.

Zimmerman, J.A., Gao, H., Abraham, F.F., 2000. Generalized stacking fault energies for embedded atom FCC metals. Model. Simul. Mater. Sci. Eng. 8 (2), 103. http://dx.doi.org/10.1088/0965-0393/8/2/302, URL http://stacks.iop.org/0965-0393/8/i=2/a=302.